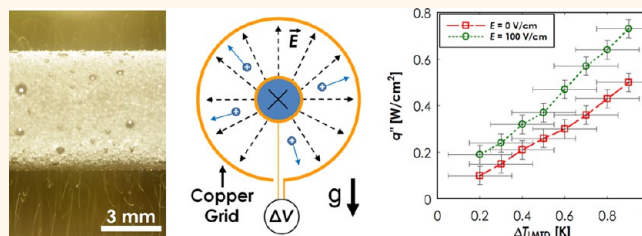


# Electric-Field-Enhanced Condensation on Superhydrophobic Nanostructured Surfaces

Nenad Miljkovic,<sup>†</sup> Daniel J. Preston,<sup>†</sup> Ryan Enright,<sup>†,\*,§</sup> and Evelyn N. Wang<sup>†,\*</sup>

<sup>†</sup>Department of Mechanical Engineering, Massachusetts Institute of Technology, 77 Massachusetts Avenue, Cambridge, Massachusetts 02139, United States, <sup>‡</sup>Thermal Management Research Group, Efficient Energy Transfer ( $\gamma$ ET) Department, Bell Laboratories Ireland, Alcatel-Lucent Ireland Ltd., Blanchardstown Business & Technology Park, Snugborough Road, Dublin 15, Ireland, and <sup>§</sup>Stokes Institute, University of Limerick, Limerick, Ireland. N.M. and E.N.W. conceived the initial idea of this research. E.N.W. guided the work. N.M., D.J.P., and R.E. fabricated and functionalized the experimental samples. N.M. and D.J.P. carried out the experiments and collected data. N.M. and D.J.P. analyzed the data. N.M. carried out the theoretical analysis. N.M. and E.N.W. were responsible for writing the paper. All authors commented on the paper.

**ABSTRACT** When condensed droplets coalesce on a superhydrophobic nanostructured surface, the resulting droplet can jump due to the conversion of excess surface energy into kinetic energy. This phenomenon has been shown to enhance condensation heat transfer by up to 30% compared to state-of-the-art dropwise condensing surfaces. However, after the droplets jump away from the surface, the existence of the vapor flow toward the condensing



surface increases the drag on the jumping droplets, which can lead to complete droplet reversal and return to the surface. This effect limits the possible heat transfer enhancement because larger droplets form upon droplet return to the surface, which impedes heat transfer until they can be either removed by jumping again or finally shedding *via* gravity. By characterizing individual droplet trajectories during condensation on superhydrophobic nanostructured copper oxide (CuO) surfaces, we show that this vapor flow entrainment dominates droplet motion for droplets smaller than  $R \approx 30 \mu\text{m}$  at moderate heat fluxes ( $q'' > 2 \text{ W/cm}^2$ ). Subsequently, we demonstrate electric-field-enhanced condensation, whereby an externally applied electric field prevents jumping droplet return. This concept leverages our recent insight that these droplets gain a net positive charge due to charge separation of the electric double layer at the hydrophobic coating. As a result, with scalable superhydrophobic CuO surfaces, we experimentally demonstrated a 50% higher overall condensation heat transfer coefficient compared to that on a jumping-droplet surface with no applied field for low supersaturations ( $< 1.12$ ). This work not only shows significant condensation heat transfer enhancement but also offers avenues for improving the performance of self-cleaning and anti-icing surfaces as well as thermal diodes.

**KEYWORDS:** condensation · wetting · superhydrophobic · nanostructured design · heat transfer enhancement · droplet charging · electric field · vapor entrainment

Vapor condensation is an essential part of energy conversion,<sup>1,2</sup> water harvesting,<sup>3,4</sup> and thermal management systems.<sup>5–10</sup> When water vapor condenses on high or low surface energy surfaces, the condensate forms a liquid film or distinct droplets, respectively. The latter, termed dropwise condensation, is desired since the condensate can be more easily removed from the surface, which significantly increases heat and mass transfer.<sup>11–13</sup> Research has focused on using a combination of roughness and chemical functionalization to create superhydrophobic surfaces<sup>14,15</sup> for dropwise condensation, whereby droplets

easily roll off the surface due to gravity upon reaching a critical size ( $\sim 2 \text{ mm}$  for water).<sup>13,16–19</sup>

A recent study showed that when small droplets ( $\sim 10\text{--}100 \mu\text{m}$ ) merge on superhydrophobic nanostructured surfaces, droplets can spontaneously eject *via* the release of excess surface energy irrespective of gravity.<sup>20</sup> Droplet removal by this jumping mechanism is highly desirable due to the increased number of small droplets,<sup>21</sup> which more efficiently transfer heat to the surface.<sup>1,22–25</sup> A number of works have since fabricated superhydrophobic nanostructured surfaces to achieve spontaneous

\* Address correspondence to enwang@mit.edu.

Received for review September 7, 2013 and accepted November 21, 2013.

Published online November 21, 2013  
10.1021/nn404707j

© 2013 American Chemical Society

droplet removal<sup>9,26–46</sup> for a variety of applications including self-cleaning,<sup>47</sup> condensation heat transfer enhancement,<sup>13,21,24,48–54</sup> thermal diodes,<sup>55,56</sup> and anti-icing.<sup>57–64</sup> Improvements of 30% in condensation heat transfer coefficients with jumping droplets as compared to state-of-the-art dropwise condensation have been demonstrated.<sup>48</sup>

However, heat transfer enhancement can be limited by droplet return due to (1) gravitational force (*i.e.*, horizontally aligned condensing surface with jumping occurring on top),<sup>20,24,48,65,66</sup> (2) entrainment in a bulk convective vapor flow occurring adjacent to the condensing surface (*i.e.*, due to buoyancy effects on vapor near the surface), and (3) entrainment in the local condensing vapor flow toward the surface (*i.e.*, the flow required for mass conservation of the condensing vapor).<sup>56</sup> Although previous studies have experimentally shown droplet return by gravity,<sup>20</sup> characterization of the vapor flow entrainment on droplet return and its effect on heat transfer is needed. An improved understanding will not only enhance heat transfer but prevent progressive surface flooding and extend high-performance condensation operational time due to the reduction in large pinned droplets on the condensing surface.

Meanwhile, we can exploit our recent discovery of positively charged jumping droplets as they leave the condensing surface due to electric double layer charge separation on the hydrophobic coating.<sup>67</sup> This insight provides a unique opportunity to utilize external electric fields to enhance droplet removal from superhydrophobic nanostructured condensing surfaces. Although external electric fields cannot increase the jumping droplet frequency because electrostatic charging occurs after droplet coalescence and departure,<sup>67</sup> they can limit droplet return to the surface caused by the three limiting mechanisms described above.

In this work, we first show *via* experiments on superhydrophobic nanostructured copper oxide (CuO) surfaces and theory that, during condensation, local vapor flow entrainment dominates droplet motion for droplets smaller than  $R \approx 30 \mu\text{m}$  at moderate heat fluxes ( $q'' > 2 \text{ W/cm}^2$ ). This process limits the condensation heat transfer coefficient for superhydrophobic jumping-droplet surfaces. Consequently, we used electric-field-enhanced (EFE) condensation, whereby an external electric field limits droplet return to the condensing surface, further enhancing heat transfer. We experimentally demonstrated that a  $\approx 50\%$  higher overall heat transfer coefficient can be achieved on scalable CuO superhydrophobic surfaces with EFE condensation compared to conventional jumping-droplet condensation, which translates to a  $\approx 100\%$  higher overall heat transfer coefficient compared to dropwise condensing copper surfaces at low supersaturations ( $S < 1.12$ ). This

work is a starting point for more advanced approaches *via* EFE condensation to improve, for example, anti-icing, self-cleaning, and thermal diode performance.

## RESULTS AND DISCUSSION

**Jumping-Droplet Return.** When a pair of equal-sized droplets coalesce and jump on a superhydrophobic nanostructured surface, they travel away from the surface in a trajectory perpendicular to the surface.<sup>20</sup> However, if the surface is oriented in such a manner as to allow jumping to occur against gravity (*i.e.*, horizontally facing upward), the returning droplet may either (1) coalesce and undergo another jump (see Supplementary Movie 1) or (2) pin to the surface and form a stationary droplet until coalescence occurs again (see Supplementary Movie 2). To eliminate gravitational return, these condensing surfaces can be oriented such that the gravitational force does not act opposite to the droplet motion; rather, it can act transverse (*i.e.*, vertical plate) or in parallel (horizontally facing downward) to the droplet. However, other mechanisms dictate the return, which we experimentally investigated.

We first characterized droplet jumping away from the surface in the direction opposite the gravitational force. We condensed water vapor on copper tubes coated with functionalized CuO nanostructures (Figure 1a; see Methods) and observed droplet jumping. The radial geometry of the tubes allowed for simultaneous high-speed imaging of droplet jumping against gravity (tube top) and with gravity (tube bottom). To visualize the behavior, the CuO tubes were tested in a controlled condensation chamber interfaced with a high-speed camera (see Supporting Information, sections S2 and S3).

Figure 1b shows a long exposure time image (50 ms) obtained during steady-state condensation on the CuO tube (see Supplementary Movie 3), where the white streaks show the trajectories of the droplets. As one might expect, droplets departing from the top of the tube returned to the tube surface, presumably due to gravitational force. However, droplets leaving the tube bottom (with gravity) sometimes returned to the bottom surface as well (Figure 1c). This return of droplets against gravity implies that either a bulk vapor flow was present that traveled upward (*i.e.*, due to buoyancy) or a local mass-conserving radial vapor flow moving toward the tube entrained droplets and caused them to return to the surface. To study the potential effect of a buoyant flow, we modified the experiment to include a flow blockage beneath the tube. Return of droplets from the bottom surface was as frequent as before, indicating that buoyancy-induced bulk vapor flow was not the mechanism of droplet return (see Supporting Information, section S4 and Movie 4).

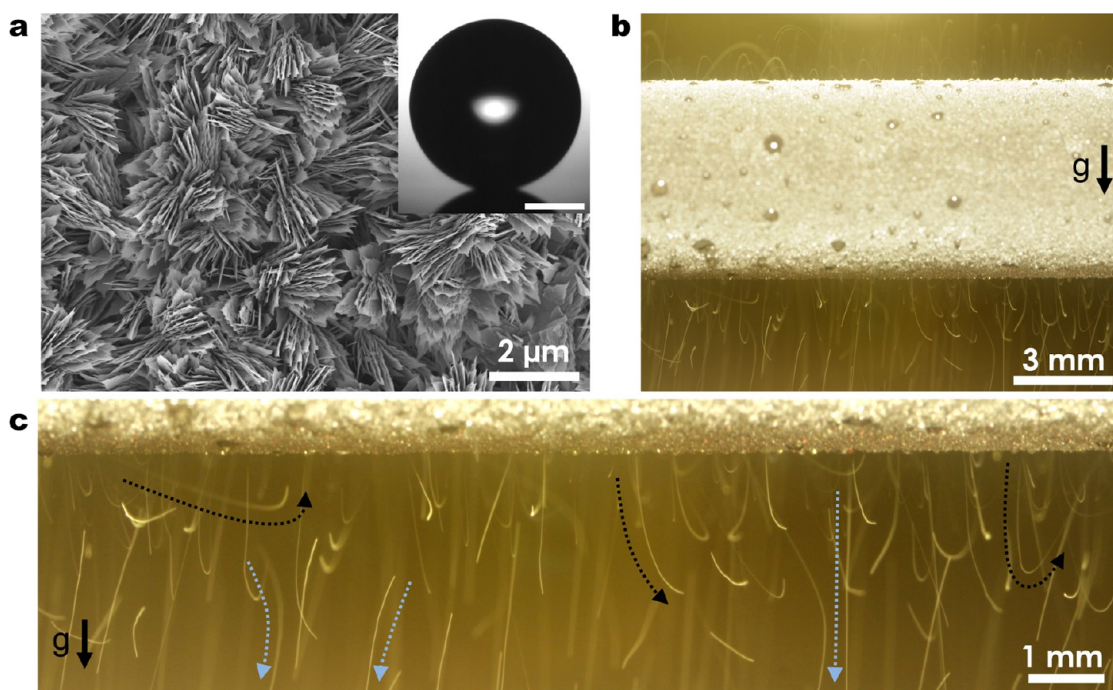


**Figure 1.** Nanostructure characterization and jumping-droplet vapor flow entrainment. (a) Field emission scanning electron micrograph (FESEM) of a 10 min oxidized CuO surface. The sharp, knife-like CuO structures have characteristic heights  $h \approx 1 \mu\text{m}$ , a solid fraction  $\varphi \approx 0.023$ , and a roughness factor  $r \approx 10$ . (Inset: Water droplet advancing contact angle on the superhydrophobic nanostructured surface,  $\theta_a = 171 \pm 3^\circ$ . Scale bar is  $20 \mu\text{m}$ .) (b) Long exposure time image (50 ms) of jumping-droplet condensation on a nanostructured CuO tube showing droplet–droplet interactions and droplet return to the bottom surface against gravity (see Supplementary Movie 3). (c) Long exposure time (50 ms) image beneath the CuO tube showing droplets jumping in the downward direction. Some droplets leave the tube (blue dotted arrows), while others are entrained by the vapor flow toward the tube surface and return (black dotted arrows). Chamber vapor pressure  $P_v = 2700 \pm 68 \text{ Pa}$ ,  $S \approx 1.02$ . The tube sample (outer diameter  $D_{OD} = 6.35 \text{ mm}$ , inner diameter  $D_{ID} = 3.56 \text{ mm}$ , and length  $W = 131 \text{ mm}$ ) was cooled via chilled water flowing inside the tube at  $5 \pm 0.25 \text{ L/min}$ ; see Supporting Information, section S2).

The second possible mechanism capable of causing droplet return is from entrainment of droplets in the local vapor flow toward the tube due to condensate mass conservation (*i.e.*, water vapor supplied to the condensing surface). To examine this hypothesis, we first modeled the radial vapor flow toward the tube to obtain the drag on departing droplets. The model was simplified by assuming that a jumping droplet departs normal to the surface directly downward in the direction of gravity. We also assumed that, due to the relatively small size of departing droplets ( $\sim 10 \mu\text{m}$ ), the shape of droplets remained spherical during flight. This assumption is justified given that the vapor density is small compared to the density of the liquid droplets ( $\rho_v \ll \rho_w$ ) and  $\text{Bo} = \rho_w g R^2 / \gamma \ll 1$ , where  $\text{Bo}$  and  $R$  are the droplet Bond number and radius ( $\approx 10 \mu\text{m}$ ), respectively,  $\rho_w$  and  $\gamma$  are the water density ( $\approx 1000 \text{ kg/m}^3$ ) and surface tension ( $\approx 72 \text{ mN/m}$ ), respectively. In addition,  $\text{We} = (\rho_v U_v^2 R) / \gamma \ll 1$  and  $\text{Ca} = \mu_v U_v / \gamma \ll 1$ , where  $\text{We}$  and  $\text{Ca}$  are the Weber and capillary numbers, respectively,  $U_v$  is the characteristic vapor velocity ( $\sim 0.1 \text{ m/s}$ ),  $\rho_v$  is the vapor density ( $\approx 0.02 \text{ kg/m}^3$ ), and  $\mu_v$  is the vapor dynamic viscosity ( $\approx 9.8 \mu\text{Pa}\cdot\text{s}$ ).<sup>68</sup> Figure 2a shows a cross-sectional schematic of the developed model with a magnified view showing the force balance on a departing droplet.

The equation of motion for the departing droplet, which includes inertia (first term), the gravitational force ( $F_g$ , second term), and the drag force due to vapor flowing in the reverse direction ( $F_D$ , third term), is

$$\frac{4}{3}\pi R^3 \rho_w \frac{dv}{dt} = \frac{4}{3}\pi R^3 g \rho_w - \frac{1}{2}\rho_v \pi R^2 C_D (v + u_v(x))^2 \quad (1)$$

where  $R$  is the droplet radius,  $v$  is the droplet velocity,  $t$  is time,  $g$  is the gravitational constant,  $C_D$  is the Reynolds number dependent drag coefficient on a sphere,<sup>69</sup> and  $u_v$  is the velocity of the vapor flow past the spherical jumping droplet. To determine the vapor velocity, mass conservation is applied to the condensing vapor. The tube heat transfer rate,  $q$  (measurable quantity), is then balanced by the energy released via vapor-to-liquid phase change:

$$\dot{m} h_{fg} = q \quad (2)$$

where  $h_{fg}$  and  $\dot{m}$  are the latent heat of vaporization and the mass flow rate toward the tube of the condensing vapor, respectively. Therefore, relating the mass flow rate to the vapor velocity gives an expression for the vapor velocity as

$$u_v(x) = \frac{R_t q''}{\rho_v (R_t + x) h_{fg}} \quad (3)$$

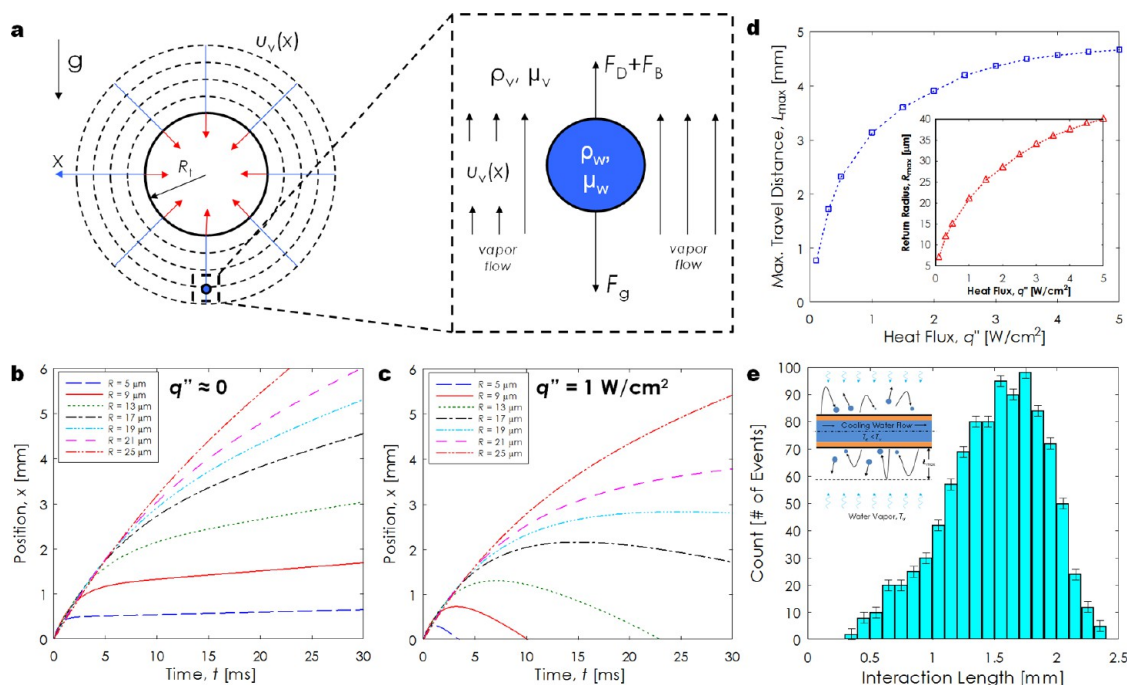


**Figure 2.** Jumping-droplet vapor flow entrainment model and experiments. (a) Schematic showing the condensing vapor flow velocity  $u_v(x)$  toward the condensing tube as a function of radial position  $x$ . The model considers only droplets traveling downward in the direction of gravity (as shown in the close-up schematic). The forces acting on the droplets are gravity ( $F_g$ ), buoyancy ( $F_B$ ), and drag due to vapor flow ( $F_D$ ) ( $R_t = 3.16$  mm). Note,  $F_B \ll F_g$  due to the large density difference between liquid water and water vapor ( $\rho_v \ll \rho_w$ ). The model was used to calculate the droplet position  $x$  beneath the tube as a function of time  $t$  for a condensing heat flux of (b)  $q'' \approx 0$  W/cm<sup>2</sup> and (c)  $q'' = 1$  W/cm<sup>2</sup>. Results show that droplets below a certain size ( $R \approx 19$   $\mu$ m, for  $q'' = 1$  W/cm<sup>2</sup>) became entrained in the condensing vapor flow and return to the tube surface. (d) Maximum travel distance,  $L_{\max}$ , a droplet can travel away from the tube prior to being returned, as a function of condensation heat flux  $q''$ . Inset: Maximum droplet radius  $R_{\max}$  corresponding to  $L_{\max}$  being returned to the condensing tube as a function of heat flux  $q''$ . At larger heat fluxes, larger droplets return due to faster condensing vapor flow and a larger drag force  $F_D$  toward the tube surface. (e) Histogram of experimentally measured droplet interaction lengths for a condensation heat flux of  $q'' \approx 0.8 \pm 0.2$  W/cm<sup>2</sup>. The interaction length is defined as the maximum distance a droplet travels before being returned to the condensing surface due to vapor flow entrainment. The experimentally measured maximum travel distance  $L_{\max, \text{exp}} \approx 2.4$  mm, which is in good agreement with the theoretically calculated value of  $L_{\max} \approx 2.5$  mm (shown in (d)).

where  $R_t$  is the condensing tube outer radius,  $x$  is the distance from the tube surface, and  $q''$  is the heat flux (heat transfer per unit area).

In order to obtain the droplet trajectory, the initial condition relating the jumping velocity ( $v_o$ ) of the droplet leaving the tube surface to the droplet radius ( $R$ ) is needed. Although a previous study experimentally determined the initial droplet velocity as a function of radius,<sup>20</sup> a hierarchical carbon nanotube surface with droplets condensing at atmospheric pressure was studied, which is distinct from our experiments carried out at low vapor pressures (<4000 Pa). To minimize uncertainties associated with the different experimental conditions, we experimentally determined the initial droplet velocity as a function of departing droplet radius. For water droplets of radii  $R \geq 2$   $\mu$ m, coalescence is governed by an inertially limited viscous regime at low neck radii ( $R_{\min}/R \leq \text{Oh}$ , where  $R_{\min}$  is the radius of the neck connecting the two coalescing droplets, and Oh is the characteristic droplet Ohnesorge number defined by  $\text{Oh} = \mu/(\rho_w \sigma R)^{1/2}$  and by an inertial regime at larger neck radii ( $R_{\min}/R > \text{Oh}$ ).<sup>70</sup> Due to the relatively low Ohnesorge number,  $\text{Oh} \approx 0.02$  to 0.1, the majority of droplet

coalescence (>90% for  $R = 2$   $\mu$ m) occurs in the inertial regime<sup>70</sup> where the time scale is governed by a capillary-inertial scaling.<sup>71–73</sup> Balancing the excess surface energy and kinetic energy of the jumping droplet,<sup>20</sup> we obtain the characteristic scaling for the droplet velocity:

$$v_o \approx \sqrt{\gamma/\rho R} \quad (4)$$

This characteristic velocity corresponds to a value of unity for the droplet Weber number,  $We = (\rho_w v_o^2 R)/\gamma = 1$ . To account for the incomplete conversion of excess surface energy to kinetic energy not captured by the scaling, we introduce a proportionality constant  $C$ , on the right-hand side of eq 4.<sup>74</sup> For our experiments on CuO at low vapor pressure ( $P_v < 4000$  Pa), eq 4 best fits the experimental data with  $C \approx 0.23$  (see Supporting Information, section S5).

Combining the initial condition (eq 4) and the vapor flow velocity (eq 3) with the droplet equation of motion (eq 1) (using a numerical discretization with a Runge–Kutta method), we determined the droplet position beneath the tube ( $x$ ) as a function of time ( $t$ ) for varying droplet radius ( $R$ ) and condensing tube heat flux ( $q''$ ) (Figure 2b,c). Figure 2b shows that when the

vapor flow velocity toward the surface is much smaller than the droplet jumping velocity ( $q'' \approx 0$ ), all droplets depart from the surface and do not return. In the absence of vapor drag, the gravitational force ensures that all droplets are removed. However, if the tube heat flux is increased to  $q'' = 1 \text{ W/cm}^2$  (Figure 2c), droplet entrainment in the condensing vapor flow becomes significant, with droplets smaller than  $R \approx 19 \mu\text{m}$  returning to the surface against gravity. In contrast, droplets larger than  $R \approx 19 \mu\text{m}$  have enough gravitational body force acting on them to depart from the surface such that they do not return from entrainment in the vapor flow. To further characterize the effects of condensate vapor flow on droplet departure, we calculated the maximum distance that the largest entrained droplets travel downward away from the tube prior to being returned to the surface ( $L_{\text{max}}$ ) as a function of condensation heat flux (Figure 2d). As the condensation heat flux increased, the maximum distance also increased due to the entrainment of progressively larger departing droplets (Figure 2d inset).

To experimentally verify our developed model, we analyzed droplet trajectories directly below the condensing tube (Figure 1c) at a heat flux of  $q'' \approx 0.8 \pm 0.2 \text{ W/cm}^2$  using high-speed imaging. For each departing droplet that returned to the surface against gravity, we measured the maximum vertical distance traveled beneath the tube prior to droplet return (interaction length). Figure 2e shows a histogram of droplet interaction lengths measured during the experiment. The maximum distance a droplet traveled away from the tube before returning to the surface was  $L_{\text{max,exp}} \approx 2.4 \text{ mm}$ , which is in excellent agreement with the model solution shown in Figure 2d, which predicted  $L_{\text{max}} \approx 2.5 \text{ mm}$  at a heat flux of  $q'' = 0.8 \text{ W/cm}^2$ . The agreement between experiments and theory indicates that droplet return (Figure 1c) is due to vapor flow entrainment.

Our experimental and model results suggest a fundamental limit to jumping-droplet condensation. Due to entrainment of departing droplets, there is a maximum attainable heat flux since larger heat fluxes result in faster vapor flow and more droplet return. As a result, this limitation presents an opportunity to utilize external body or surface forces to further aid droplet removal from the surface at high fluxes, whether from forced convection,<sup>75–77</sup> Marangoni stresses,<sup>78</sup> or electrostatic fields.<sup>67</sup> We have chosen to use electric fields due to our recent discovery that jumping droplets also gain a positive electrostatic charge as they leave the condensing surface due to electric double layer charge separation on the hydrophobic coating.<sup>67</sup> Exploiting this electrostatic charge using external electric fields provides a unique and easily implementable approach to enhance droplet removal from superhydrophobic nanostructured condensing surfaces.

### Electric Field Manipulation of Charged Jumping Droplets.

With our new understanding of the limitations for droplet removal due to vapor flow entrainment, we developed EFE condensation. Our recent study on charged jumping droplets provides an avenue for creating an external body force on departing droplets in opposition to the drag force. To prevent entrainment, we used an external electrode biased to attract positively charged departing droplets.<sup>67</sup> Figure 3a and b depict the EFE condensation concept, where a copper electrode placed beneath the tube was voltage biased with 0 and 500 V (electrode is negative, tube is grounded, 40 ms exposure time), respectively, to form an electric field in order to prevent the return of jumping droplets (see Supporting Information, section S6). Under the no-field condition, droplets smaller than  $R_{\text{max}}$  jumped downward and then returned to the surface, as seen by the changing trajectories in the long exposure time image (Figure 3a). However, when the field strength was large enough, droplet reversal was completely eliminated (Figure 3b) and potentially higher heat transfer could be attained due to the reduction in average droplet size distribution on the condensing surface.<sup>24,48,66,79</sup>

To study the effect of external electric fields, we modified our experimental setup to include a copper wire cage electrode surrounding the condensing superhydrophobic CuO tube (Figure 3c–e). By applying a voltage between the grounded tube and wire cage, droplets jumping from the surface were attracted toward the cage and away from the surface, limiting droplet return due to entrainment.

Figure 4 shows long exposure (40 ms) time-lapse images of condensation with a positive surface voltage bias (grounded tube, negative cage). Increasing voltages resulted in decreasing droplet return, as shown by fewer parabolic trajectories on top of the tube surface which indicate droplets returning to the condensing surface. At low voltages ( $\Delta V < 100 \text{ V}$ ), droplet return was decreased when compared to no-field condensation, but was still present (Figure 4a,b,c). Droplet return was not eliminated until a critical voltage of  $\Delta V \approx 130 \text{ V}$  was reached, corresponding to a critical electric field strength of approximately  $E \approx \Delta V / (R_o - R_t) \approx 75 \text{ V/cm}$ , where  $R_o$  is the cage radius ( $\approx 2 \text{ cm}$ ).

To theoretically estimate the critical electric field and better understand the EFE droplet removal mechanism, we can compare the forces on a departed droplet just as it reaches the crest of its motion and is about to reverse direction ( $v_v = 0$ , where  $v$  is the droplet velocity).

The gravitational force acting on the droplet can be estimated by  $F_g = (4/3)\pi R^3 \rho_w g \approx 0.04 \text{ nN}$ , where  $R$  is the characteristic jumping droplet radius ( $R \approx 10 \mu\text{m}$ ).<sup>13,48</sup> The vapor drag force can be estimated by considering conservation of condensate vapor mass to calculate the

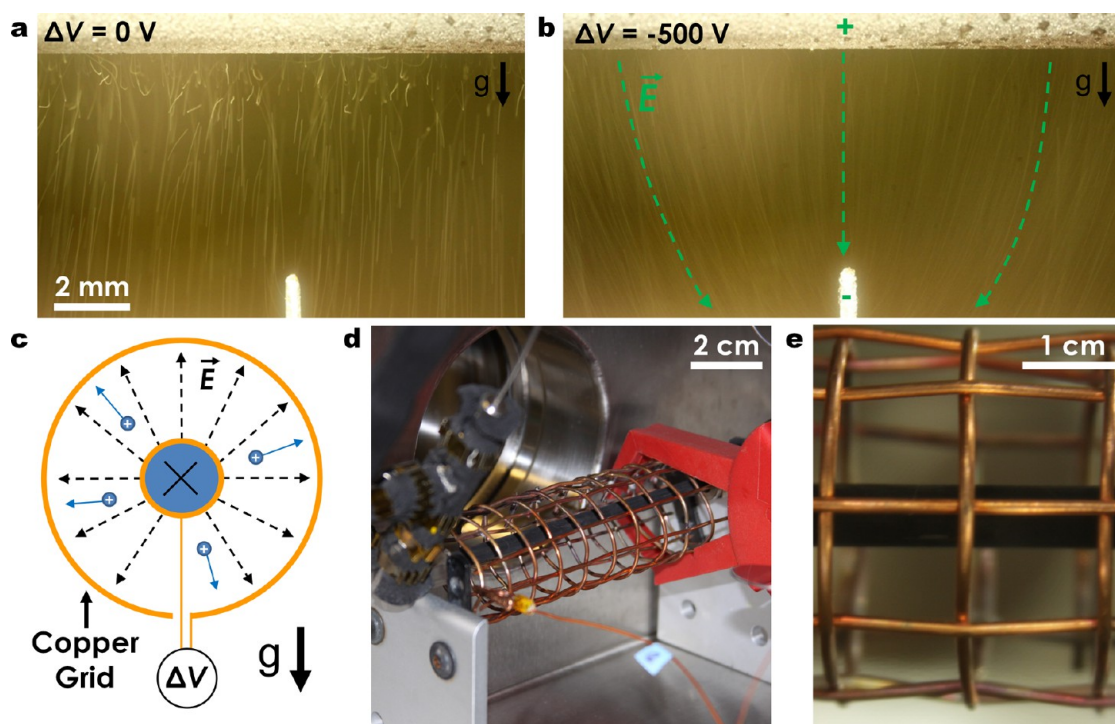


**Figure 3.** Electric-field-enhanced droplet removal. Long exposure time image (40 ms) of water vapor condensation on a superhydrophobic CuO tube with a copper electrode located beneath with (a) zero bias voltage having significant droplet–droplet interactions and return to the surface against gravity and (b) 500 V bias (electrode negative, tube ground, green dotted arrows represent the electric field lines). The image shows the concept of electric-field-enhanced (EFE) condensation with no droplet return to the surface and significant attraction of jumping droplets away from the surface ( $P_v = 2700 \pm 75$  Pa,  $S \approx 1.04$ ). (c) Schematic of EFE condensation. The outer copper grid is biased negative relative to the condensing tube, creating an electric field and attracting jumping droplets away from the surface and preventing droplet return due to vapor flow entrainment. Images of the EFE condensation experiment showing (d) isometric and (e) front views from the camera viewport. The outer copper grid is biased negative relative to the condensing tube, creating an electric field and attracting jumping droplets away from the surface.

vapor velocity  $U_v \approx q''/(\rho_v h_{fg})$ , where  $U_v$  is the characteristic vapor flow velocity toward the tube,  $q''$  is the characteristic heat flux ( $q'' \approx 0.5$  W/cm<sup>2</sup>), and  $h_{fg}$  is the water latent heat of vaporization ( $h_{fg} = 2260$  kJ/kg). By substituting values for our experimental conditions, we obtain a characteristic water vapor velocity of  $U_v \approx 0.1$  m/s.

To determine the characteristic drag force on the droplet due to the vapor, the Stokes flow approximation was used, which is appropriate due to the low Reynolds numbers,  $Re$ , of the droplet motion. The  $Re = [\rho_v U_v (2R)]/\mu_v \approx 0.005$ , where  $R$  is the characteristic jumping droplet radius ( $R \approx 10$  μm). Using the Stokes approximation yields a characteristic Stokes drag,<sup>80</sup>  $F_{drag} = 6\pi\mu_v U_v R \approx 0.19$  nN. In order to calculate our minimum critical electric field, we equate the difference between the characteristic Stokes drag and the gravitational force (droplet jumping downward, Figure 2a) to the force imparted by an external field on the charged droplet,  $E_{crit} \approx (F_{drag} - F_g)/q$ , where  $q$  is the electrostatic charge on the droplet<sup>67</sup> ( $q \approx 15$  fC). Substituting in our values, we obtain a critical field strength of  $E_{crit} \approx 100$  V/cm, which is in reasonable agreement with the experimentally determined critical value of  $\approx 75$  V/cm.

It is important to note that the estimated characteristic electric field in these experiments is assumed to equal the form of two uniformly spaced parallel plates,  $E \approx \Delta V/(R_o - R_i)$ . Although a reasonable approximation, the field between the wire cage and tube is better represented by a radially dependent electric field encountered between two concentric cylinders, which can be expressed as  $E_r \approx \Delta V/[\ln(R_o/R_i)r]$ , where  $r$  is the radial distance from the tube centerline. To estimate the accuracy of our approximation, we calculated the two limits of electric field strength (at the CuO tube surface and the copper wire mesh surface) and found  $35.3 < E_r < 222.5$  V/cm, which bounds the estimated critical electric field of  $E \approx \Delta V/(R_o - R_i) \approx 75$  V/cm.

Figure 5a and b show long exposure (40 ms) time-lapse images of no-field and EFE condensation, respectively. We found that as the condensation time approached 8 min, the no-field jumping-droplet condensation mode (Figure 5a) had a larger population of pinned liquid droplets on the surface. Although droplet jumping was still present at later times ( $t > 10$  min), progressive flooding of the surface due to return of departing droplets from vapor flow entrainment created a larger maximum droplet size ( $R_{max,no-field} \approx 145 \pm 29$  μm, Figure 5c). In contrast to no-field droplet

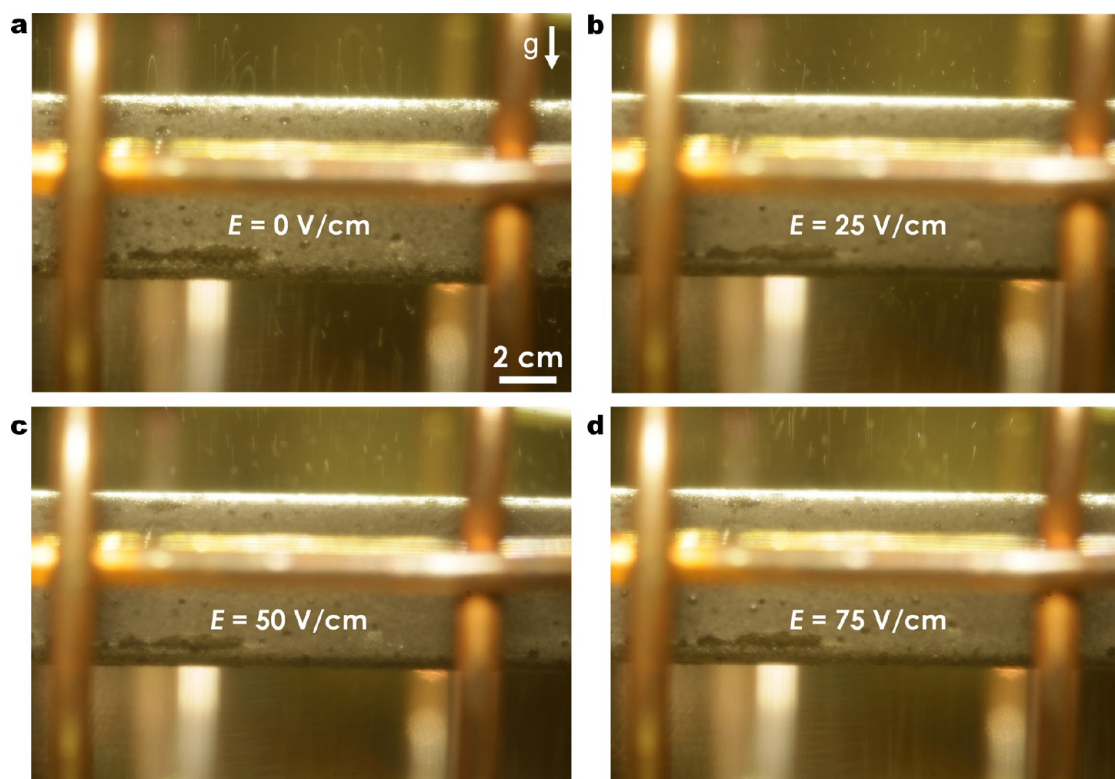


**Figure 4.** EFE condensation droplet removal dynamics. Long exposure time images (40 ms) of EFE condensation with (a)  $E = 0$  V/cm, (b)  $E = 25$  V/cm, (c)  $E = 50$  V/cm, and (d)  $E = 75$  V/cm. The outer copper grid (Figure 3c–e) is biased negative relative to the condensing tube. Increasing voltage results in fewer droplets returning to the condensing tube surface. This is shown via the reduction in parabolic droplet streaks (trajectories) on the top of the tube surface from (a) to (d). Electric fields larger than  $E \approx 75$  V/cm had identical performance (all jumping droplets were removed), indicating that the critical electric field force on the droplet was reached and was large enough to overcome vapor drag at this particular heat flux ( $P_v = 2700 \pm 75$  Pa,  $S \approx 1.04$ ).

jumping, the EFE condensing mode (Figure 5b) showed little increase in maximum droplet size on the surface through the experiment ( $R_{\text{max,EFE}} < 25 \pm 8$   $\mu\text{m}$ , Figure 5c). This observation implies that EFE condensation provides a means to further increase jumping-droplet heat transfer by minimizing the average droplet size and increasing the population of small droplets on the surface, which are more effective at transferring heat during condensation.<sup>66,79</sup>

It is important to note that although charged jumping droplets feel an attractive Coulombic force toward the tube at all times (due to opposite charge left on the hydrophobic coating), the magnitude of the force is negligible compared to the drag force at the length scales ( $\sim 1$  mm) of droplet deceleration and reversal.<sup>67</sup> In addition, the progressive flooding mechanism is distinct from the nucleation-density-mediated flooding mechanism<sup>48</sup> (see Supporting Information, section S7). Nucleation-density-mediated flooding occurs due to nucleation site activation (at elevated supersaturations,  $S > 1.12$ ), droplet coalescence within the structure, and filling of the structure with condensate. Progressive flooding occurs due to the progressive return of jumping droplets back to the surface due to vapor flow entrainment and gravity. These returning droplets do not necessarily jump again

and remain adhered to the surface (see Supplementary Movie 2), increasing the time average droplet size and degrading overall heat transfer performance.

**Heat Transfer Theory and Experiments.** To study the impact of the gradual increase in average droplet size on the condensing surface, *i.e.*, progressive flooding, we used our previously developed model that incorporates thermal resistance-based droplet growth, the emergent droplet wetting morphology, and droplet distribution theory (see Supporting Information, section S8).<sup>24,66</sup> Figure 6a shows the normalized condensation heat transfer coefficient ( $\bar{h}_{\text{Re}}/\bar{h}_{\text{Re}=5\mu\text{m}}$ ) as a function of maximum droplet departure diameter,  $R_e$ . The normalization factor is a condensation heat transfer coefficient for a jumping droplet surface with a departure diameter of  $R_e = 5$   $\mu\text{m}$ , which serves as an upper bound for heat transfer performance from previously observed experiments where the minimum droplet departure size on the CuO nanostructures is  $\sim 5$   $\mu\text{m}$ .<sup>25,48</sup> As the droplet departure radius increased, the condensation heat transfer degraded (Figure 6a inset) due to the presence of larger droplets on the surface whose growth is heat conduction limited.<sup>66</sup> The results show that increasing the departure size from  $R_e = 5$   $\mu\text{m}$  to  $R_e = 10$   $\mu\text{m}$  degraded the condensation performance by as much as 20%, indicating the

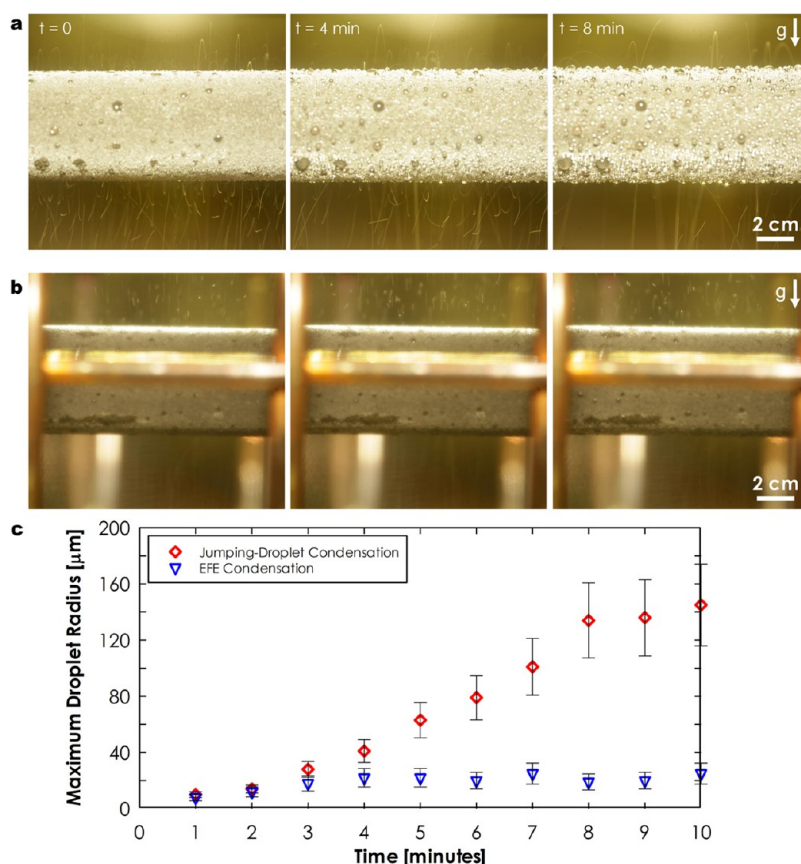


**Figure 5.** Progressive flooding due to vapor flow entrainment. Time-lapse (long exposure time, 40 ms) images of steady state (a) jumping-droplet condensation and (b) EFE condensation with  $E = 75$  V/cm ( $P_v = 2700 \pm 75$  Pa,  $S \approx 1.04$ ). Jumping-droplet condensation with no electric field shows significant droplet return to the surface due to vapor flow entrainment. As droplets return, some may coalesce and jump again (see Supplementary Movie 1), while others may remain pinned to the surface (see Supplementary Movie 2). As time progressed ( $t \rightarrow 8$  min), the average droplet size on the surface increased and limited heat transfer performance for jumping-droplet condensation with no applied electric field. (c) Maximum droplet radius on the condensing surface as a function of time for jumping-droplet and EFE condensation. For EFE condensation, the efficient removal of jumping droplets and prevention of return due to vapor flow entrainment *via* the electric field ensured a large and steady population of small droplets ( $R < 25$   $\mu\text{m}$ ), which are more effective at removing heat during condensation.

importance of eliminating progressive flooding and droplet return for optimum performance.

To experimentally quantify the effect of eliminating droplet return and progressive flooding, we measured the overall heat transfer coefficient ( $\bar{U}$ ) for varying electric fields ( $E = 0, 25, 100,$  and  $200$  V/cm) (see Supporting Information, section S2). Figure 6b shows the overall surface heat flux as a function of the log-mean-temperature-difference ( $\Delta T_{\text{LMTD}}$ ) between the saturated vapor and cooling water. Relatively low cooling water flow rates of  $0.5 \pm 0.025$  L/min were used in the experiments to increase the temperature difference from inlet to outlet and obtain a greater signal-to-noise ratio. However, reducing the flow rate led to relatively low overall heat transfer coefficients due to the larger convective resistance on the coolant side.

Figure 6b shows that for the case of no electric field the overall heat transfer coefficient was approximately  $\approx 0.51 \pm 0.14$  W/cm<sup>2</sup>·K. However, by applying electric fields of  $E = 100$  V/cm and  $200$  V/cm, the heat transfer coefficient increased by approximately 50% to  $0.77 \pm$

$0.12$  W/cm<sup>2</sup>·K for both cases. The independence of heat transfer performance on electric field strength (100 or 200 V/cm) was consistent with exceeding the critical field strength ( $E \approx 75$  V/cm), which resulted in efficient removal of all jumping droplets. Note that the no-field overall heat transfer coefficient is lower than the value previously reported ( $\bar{U}_{\text{jumping}} = 1.65 \pm 0.22$  W/cm<sup>2</sup>·K)<sup>48</sup> due to the lower internal cooling water flow rate used in these experiments in order to achieve a larger inlet-to-outlet temperature difference and signal-to-noise ratio. In addition, higher condensation heat fluxes ( $S > 1.04$ ,  $q'' > 1$  W/cm<sup>2</sup>) were not studied in order to minimize the effect of progressive flooding due to vapor flow entrainment (which occurred during no-field jumping-droplet condensation; see Supporting Information, section S7) and allow for a direct comparison between jumping-droplet condensation with and without an external electric field. Furthermore, at higher supersaturations ( $S > 1.12$ ,  $q'' > 8$  W/cm<sup>2</sup>) for EFE condensation, nucleation-density-mediated flooding of the surface remained,<sup>49</sup> as

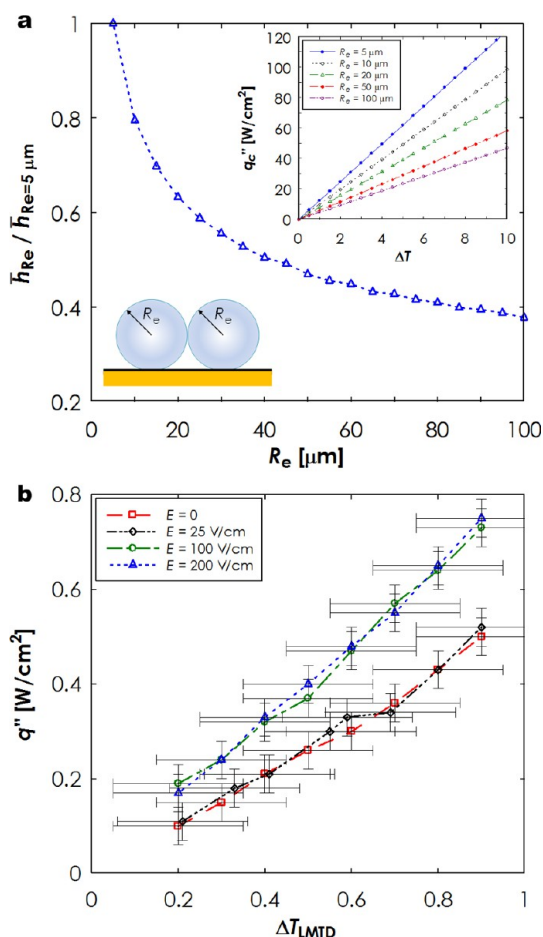


**Figure 6.** Theoretical and experimental heat transfer performance of EFE condensation. (a) Theoretical condensation heat transfer coefficient ratio ( $\bar{h}_{Re}/\bar{h}_{Re=5\mu m}$ ) of a surface undergoing jumping-droplet condensation as a function of droplet departure radius  $R_e$ . Inset: Condensation heat flux ( $q_c''$ ) as a function of surface to vapor temperature difference ( $\Delta T$ ) for different departure radii ( $5\mu m < R_e < 100\mu m$ ). As expected, the heat transfer coefficient ratio and heat flux decrease as  $R_e$  increases due to the presence of larger droplets on the surface, which are conduction limited. (b) Experimental steady-state overall surface heat flux ( $q''$ ) as a function of log mean water-to-vapor temperature difference ( $\Delta T_{LMTD}$ ) for tube surfaces undergoing jumping-droplet condensation and EFE condensation (CuO chemical oxidation time  $\tau = 10$  min, chamber vapor pressure  $P_v = 2700 \pm 68$  Pa,  $1.02 < S \leq 1.04$ , chilled water flow rate inside the tube  $\approx 0.5 \pm 0.025$  L/min). Faster droplet removal and reduction of droplet return when an external electric field larger than the critical electric field ( $E \approx 75$  V/cm) was applied resulted in the highest heat fluxes for the EFE jumping samples. Error bars denote the propagation of error associated with the inlet-to-outlet cooling fluid temperature difference ( $\pm 0.08$  °C), mass flow rate ( $\pm 5\%$ ), and pressure ( $\pm 2.5\%$ ).

previously observed on superhydrophobic CuO surfaces.<sup>25,48</sup> The nucleation-density-mediated flooding mechanism was found to be independent of the electric field strength, which indicates that, for the voltage range explored, electric fields cannot remove more droplets than would have already departed. This result agrees well with theory since the electric field can act on droplets only once they have attained an

electrostatic charge by coalescing and leaving the surface.<sup>67</sup> This result is in contrast to the progressive flooding mechanism, which is governed by vapor entrainment and is sensitive to both the condensation heat flux (tube inlet-to-outlet temperature difference) and electric field strength. The larger the tube inlet-to-outlet temperature difference, the higher the condensation heat flux and the larger the vapor flow rate and entrainment of jumping droplets. To counter the larger entrainment force, a larger electric field should be applied to limit droplet return to the surface.

The outcomes of this work support the findings that vapor flow entrainment is a performance-limiting phenomena during jumping-droplet condensation and that efficient droplet removal is critical in realizing enhanced condensation heat and mass transfer over state-of-the-art dropwise condensing surfaces. The experimental results suggest that, although EFE condensation on superhydrophobic surfaces has the ability to enhance condensation performance, these surfaces cannot currently be used for high heat flux applications due to nucleation-density-mediated flooding of the surface.<sup>25,48,49</sup>

In the future, it would be interesting to investigate different surface geometries with uniform vapor flow velocities (*i.e.*, flat plate heat exchangers) to identify optimum EFE condenser designs. In addition, alternate methods of creating electric fields *via* positively biased embedded electrodes beneath the condensing surface<sup>81</sup> (which would repel jumping droplets as opposed to attracting them with an external electrode) promise to be attractive alternatives to using external electrodes to prevent potential condensate bridging (short-circuiting). Furthermore, although not studied here, condensate management and recycling after reaching the external electrode needs to be considered. Two potential methods involve (a) the use of highly wettable wicking electrode materials (*i.e.*, a porous copper grid), which can transport the condensate toward the tube ends to a condensate reservoir,<sup>82–85</sup> where it can be recycled, and (b) the use of geometry (*i.e.*, the condensing surface and electrode are parallel vertical plates) such that gravitational removal of the condensate from the electrode could be achieved.

## CONCLUSIONS

In summary, we demonstrated that the vapor drag toward the condensing surface acts as a barrier to heat transfer performance of superhydrophobic surfaces with jumping droplets. Through experiments and modeling, we showed that the entrainment and return of jumping droplets results in the progressive flooding of the condensing surface that is characterized by the gradual increase in average droplet size and gradual deterioration of condensation heat transfer performance. To counteract the vapor drag, we leveraged our knowledge of droplet charging in conjunction with external

electric fields to demonstrate a new mode of condensation called electric-field-enhanced condensation. As a result, 50% higher overall heat transfer coefficients were obtained at electric fields of 100 and 200 V/cm compared to typical (no-field) jumping-droplet surfaces. At high supersaturations ( $S > 1.12$ ), however, nucleation-density-mediated flooding of the nanostructured surfaces still led to the formation of highly pinned droplets, which

degraded the condensation heat transfer coefficient. These results provide guidelines for the fabrication of high-performance nanostructured surfaces for moderate condensation heat flux applications. Furthermore, this work demonstrates new opportunities for EFE condensation to enhance heat transfer,<sup>48</sup> anti-icing,<sup>57</sup> self-cleaning performance,<sup>47</sup> and thermal diode efficiency.<sup>55,56</sup>

## METHODS

**Fabrication.** To create the CuO nanostructures (Figure 1a), commercially available oxygen-free copper tubes were used (99.9% purity) with outer diameters  $D_{OD} = 6.35$  mm, inner diameters  $D_{ID} = 3.56$  mm, and lengths  $W = 131$  mm, as the test samples for the experiments. Each copper tube was cleaned in an ultrasonic bath with acetone for 10 min and rinsed with ethanol, isopropyl alcohol, and deionized (DI) water. The tubes were then dipped into a 2.0 M hydrochloric acid solution for 10 min to remove the native oxide film on the surface, then triple-rinsed with DI water and dried with clean nitrogen gas. Nanostructured CuO films were formed by immersing the cleaned tubes (with ends capped) into a hot ( $96 \pm 3$  °C) alkaline solution composed of  $\text{NaClO}_2$ , NaOH,  $\text{Na}_3\text{PO}_4 \cdot 12\text{H}_2\text{O}$ , and DI water (3.75:5:10:100 wt %).<sup>86</sup> During the oxidation process, a thin ( $\approx 300$  nm)  $\text{Cu}_2\text{O}$  layer was formed that then reoxidized to form sharp, knife-like CuO oxide structures with heights of  $h \approx 1$   $\mu\text{m}$ , a solid fraction  $\phi \approx 0.023$ , and a roughness factor  $r \approx 10$ .

**Functionalization.** TFSTs (trichloro(1H,1H,2H,2H-perfluorooctyl)silane, Sigma) was deposited from the vapor phase. Prior to silane deposition, each tube was oxygen plasma cleaned for 2 h to remove organic contaminants on the surface. Once clean, the tube samples were immediately placed in a vacuum desiccator (06514-10, Cole Parmer) with a small amount of liquid silane. The desiccator was evacuated by a roughing pump for 2 min to a minimum pressure of  $\sim 2$  kPa. A valve was then closed to isolate the pump from the desiccator, and the sample was held in a vacuum ( $\sim 2$  kPa) for another 7 min. The functionalized tubes were then rinsed in ethanol and DI water and dried in a clean nitrogen stream. The coating had a typical advancing angle of  $\theta_a \approx 120^\circ$  when measured on a smooth reference surface and typical advancing/receding angles of  $\theta_a/\theta_r \approx 171^\circ/167 \pm 3^\circ$  when measured on the nanostructured CuO surface.

**Surface Characterization.** Advancing and receding contact angles for all samples were measured and analyzed using a microgoniometer (MCA-3, Kyowa Interface Science Co., Japan). Field emission electron microscopy was performed on a Zeiss Ultra Plus FESEM (Carl Zeiss GMBH) at an imaging voltage of 3 kV.

**Conflict of Interest:** The authors declare no competing financial interest.

**Acknowledgment.** We gratefully acknowledge funding support from the MIT S3TEC Center, an Energy Frontier Research Center funded by the Department of Energy, Office of Science, Basic Energy Sciences, under Award DE-FG02-09ER46577, and the Office of Naval Research (ONR) with Dr. Mark Spector as program manager. D.J.P. acknowledges funding received by the National Science Foundation Graduate Research Fellowship under Grant No. 1122374. Any opinion, findings, conclusions, or recommendations expressed in this material are those of the author(s) and do not necessarily reflect the views of the National Science Foundation. R.E. acknowledges funding received from the Irish Research Council for Science, Engineering, and Technology, cofunded by Marie Curie Actions under FP7. We also acknowledge the support from the National Science Foundation through the Major Research Instrumentation Grant for Rapid Response Research (MRI-RAPID) for the microgoniometer.

**Supporting Information Available:** Four videos showing the jumping-droplet and condensation processes, as well as

further information on the condensation chamber setup, data collection methodology, the effect of bulk vapor flow, jumping-droplet initial velocity, jumping-droplet interaction with electric fields, flooding mechanisms, and heat transfer modeling. This material is available free of charge via the Internet at <http://pubs.acs.org>.

## REFERENCES AND NOTES

- Glicksman, L. R.; Hunt, A. W. Numerical Simulation of Dropwise Condensation. *Int. J. Heat Mass Transfer* **1972**, *15*, 2251–2269.
- Thomas, D. H.; United States Environmental Protection Agency; Oak Ridge National Laboratory. *Energy Efficiency through Combined Heat and Power or Cogeneration*; Nova Science Publishers: New York, NY, 2010.
- Love, J. C.; Estroff, L. A.; Kriebel, J. K.; Nuzzo, R. G.; Whitesides, G. M. Self-Assembled Monolayers of Thiolates on Metals as a Form of Nanotechnology. *Chem. Rev.* **2005**, *105*, 1103–1169.
- Andrews, H. G.; Eccles, E. A.; Schofield, W. C. E.; Badyal, J. P. S. Three-Dimensional Hierarchical Structures for Fog Harvesting. *Langmuir* **2011**, *27*, 3798–3802.
- Miljkovic, N.; Wang, E. N. Modeling and Optimization of Hybrid Solar Thermoelectric Systems with Thermosyphons. *Sol. Energy* **2011**, *85*, 2843–2855.
- Leach, R. N.; Stevens, F.; Langford, S. C.; Dickinson, J. T. Dropwise Condensation: Experiments and Simulations of Nucleation and Growth of Water Drops in a Cooling System. *Langmuir* **2006**, *22*, 8864–8872.
- Rykaczewski, K.; Scott, J. H. J.; Rajauria, S.; Chinn, J.; Chinn, A. M.; Jones, W. Three Dimensional Aspects of Droplet Coalescence during Dropwise Condensation on Superhydrophobic Surfaces. *Soft Matter* **2011**, *7*, 8749–8752.
- Milani, D.; Abbas, A.; Vassallo, A.; Chiesa, M.; Al Bakri, D. Evaluation of Using Thermoelectric Coolers in a Dehumidification System to Generate Freshwater from Ambient Air. *Chem. Eng. Sci.* **2011**, *66*, 2491–2501.
- Chen, X.; Wu, J.; Ma, R.; Hua, M.; Koratkar, N.; Yao, S.; Wang, Z. Nanograsped Micropyramidal Architectures for Continuous Dropwise Condensation. *Adv. Funct. Mater.* **2011**, *21*, 4617–4623.
- Xiao, R.; Miljkovic, N.; Enright, R.; Wang, E. N. Immersion Condensation on Oil-Infused Heterogeneous Surfaces for Enhanced Heat Transfer. *Sci. Rep.* **2013**, *3*, 1988.
- Schmidt, E.; Schurig, W.; Sellschopp, W. Versuche über die Kondensation von Wasserdampf in Film- und Tropfenform. *Forsch. Ingenieurwes.* **1930**, *1*, 53–63.
- Rose, J. W. Dropwise Condensation Theory and Experiment: A Review. *Proc. Inst. Mech. Eng., Part A* **2002**, *216*, 115–128.
- Miljkovic, N.; Wang, E. N. Condensation Heat Transfer on Superhydrophobic Surfaces. *MRS Bull.* **2013**, *38*, 397–406.
- Quere, D. Wetting and Roughness. *Annu. Rev. Mater. Res.* **2008**, *38*, 71–99.
- Lafuma, A.; Quere, D. Superhydrophobic States. *Nat. Mater.* **2003**, *2*, 457–460.
- Dimitrakopoulos, P.; Higdon, J. J. L. On the Gravitational Displacement of Three-Dimensional Fluid Droplets from Inclined Solid Surfaces. *J. Fluid Mech.* **1999**, *395*, 181–209.

17. Kim, S.; Kim, K. J. Dropwise Condensation Modeling Suitable for Superhydrophobic Surfaces. *J. Heat Transfer* **2011**, *133*, 081502.
18. Kim, H. Y.; Lee, H. J.; Kang, B. H. Sliding of Liquid Drops Down an Inclined Solid Surface. *J. Colloid Interface Sci.* **2002**, *247*, 372–380.
19. Enright, R.; Miljkovic, N.; Alvarado, J. L.; Kim, K. J.; Rose, J. W. Dropwise Condensation on Micro- and Nanostructured Surfaces. *Nanoscale and Microscale Thermophys. Eng.* **2013**, DOI: 10.1080/15567265.2013.862889.
20. Boreyko, J. B.; Chen, C. H. Self-Propelled Dropwise Condensate on Superhydrophobic Surfaces. *Phys. Rev. Lett.* **2009**, *103*, 184501.
21. Dietz, C.; Rykaczewski, K.; Fedorov, A. G.; Joshi, Y. Visualization of Droplet Departure on a Superhydrophobic Surface and Implications to Heat Transfer Enhancement during Dropwise Condensation. *Appl. Phys. Lett.* **2010**, *97*, 033104.
22. Graham, C.; Griffith, P. Drop Size Distributions and Heat Transfer in Dropwise Condensation. *Int. J. Heat Mass Transfer* **1973**, *16*, 337–346.
23. Rose, J. W. On the Mechanism of Dropwise Condensation. *Int. J. Heat Mass Transfer* **1967**, *10*, 755–762.
24. Miljkovic, N.; Enright, R.; Wang, E. N. Effect of Droplet Morphology on Growth Dynamics and Heat Transfer during Condensation on Superhydrophobic Nanostructured Surfaces. *ACS Nano* **2012**, *6*, 1776–1785.
25. Enright, R.; Miljkovic, N.; Dou, N.; Nam, Y.; Wang, E. N. Condensation on Superhydrophobic Copper Oxide Nanostructures. *J. Heat Transfer* **2013**, *135*, 091304.
26. Chen, C. H.; Cai, Q. J.; Tsai, C. L.; Chen, C. L.; Xiong, G. Y.; Yu, Y.; Ren, Z. F. Dropwise Condensation on Superhydrophobic Surfaces with Two-Tier Roughness. *Appl. Phys. Lett.* **2007**, *90*, 173108.
27. Dietz, C.; Rykaczewski, K.; Fedorov, A.; Joshi, Y. ESEM Imaging of Condensation on a Nanostructured Superhydrophobic Surface. *J. Heat Transfer* **2010**, *132*, 080904.
28. Varanasi, K. K.; Hsu, M.; Bhate, N.; Yang, W. S.; Deng, T. Spatial Control in the Heterogeneous Nucleation of Water. *Appl. Phys. Lett.* **2009**, *95*, 094101.
29. Miljkovic, N.; Enright, R.; Maroo, S. C.; Cho, H. J.; Wang, E. N. Liquid Evaporation on Superhydrophobic and Superhydrophilic Nanostructured Surfaces. *J. Heat Transfer* **2011**, *133*, 080903.
30. Lau, K. K. S.; Bico, J.; Teo, K. B. K.; Chhowalla, M.; Amarantunga, G. A. J.; Milne, W. I.; McKinley, G. H.; Gleason, K. K. Superhydrophobic Carbon Nanotube Forests. *Nano Lett.* **2003**, *3*, 1701–1705.
31. Miljkovic, N.; Preston, D. J.; Enright, R.; Adera, S.; Nam, Y.; Wang, E. N. Jumping Droplet Dynamics on Scalable Nanostructured Superhydrophobic Surfaces. *J. Heat Transfer* **2013**, *135*, 080907.
32. Miljkovic, N.; Xiao, R.; Preston, D. J.; Enright, R.; McKay, I.; Wang, E. N. Condensation on Hydrophilic, Hydrophobic, Nanostructured Superhydrophobic and Oil-Infused Surfaces. *J. Heat Transfer* **2013**, *135*, 080906.
33. Rykaczewski, K. Microdroplet Growth Mechanism during Water Condensation on Superhydrophobic Surfaces. *Langmuir* **2012**, *28*, 7720–7729.
34. Rykaczewski, K.; Paxson, A. T.; Anand, S.; Chen, X.; Wang, Z.; Varanasi, K. K. Multimode Multidrop Serial Coalescence Effects during Condensation on Hierarchical Superhydrophobic Surfaces. *Langmuir* **2013**, *29*, 881–891.
35. Rykaczewski, K.; Scott, J. H. J.; Fedorov, A. G. Electron Beam Heating Effects during Environmental Scanning Electron Microscopy Imaging of Water Condensation on Superhydrophobic Surfaces. *Appl. Phys. Lett.* **2011**, *98*, 093106.
36. Rykaczewski, K.; Osborn, W. A.; Chinn, J.; Walker, M. L.; Scott, J. H. J.; Jones, W.; Hao, C.; Yaod, S.; Wang, Z. How Nanorough Is Rough Enough to Make a Surface Superhydrophobic during Water Condensation? *Soft Matter* **2012**, *8*, 8786–8794.
37. He, M.; Zhou, X.; Zeng, X. P.; Cui, D. P.; Zhang, Q. L.; Chen, J.; Li, H. L.; Wang, J. J.; Cao, Z. X.; Song, Y. L.; *et al.* Hierarchically Structured Porous Aluminum Surfaces for High-Efficient Removal of Condensed Water. *Soft Matter* **2012**, *8*, 6680–6683.
38. Feng, J.; Pang, Y.; Qin, Z.; Ma, R.; Yao, S. Why Condensate Drops Can Spontaneously Move Away on Some Superhydrophobic Surfaces but Not on Others. *ACS Appl. Mater. Interfaces* **2012**, *4*, 6618–6625.
39. Feng, J.; Qin, Z. Q.; Yao, S. H. Factors Affecting the Spontaneous Motion of Condensate Drops on Superhydrophobic Copper Surfaces. *Langmuir* **2012**, *28*, 6067–6075.
40. Lv, C. J.; Hao, P. F.; Yao, Z. H.; Song, Y.; Zhang, X. W.; He, F. Condensation and Jumping Relay of Droplets on Lotus Leaf. *Appl. Phys. Lett.* **2013**, *103*, 021601.
41. Lo, C.-W.; Wang, C.-C.; Lu, M.-C. Spatial Control of Heterogeneous Nucleation on the Superhydrophobic Nanowire Array. *Adv. Funct. Mater.* **2013**, DOI: 10.1002/adfm.201301984.
42. Narhe, R. D.; Khandkar, M. D.; Shelke, P. B.; Limaye, A. V.; Beysens, D. A. Condensation-Induced Jumping Water Drops. *Phys. Rev. E* **2009**, *80*, 031604.
43. Liu, T. Q.; Sun, W.; Sun, X. Y.; Ai, H. R. Mechanism Study of Condensed Drops Jumping on Superhydrophobic Surfaces. *Colloids Surf., A* **2012**, *414*, 366–374.
44. Nam, Y.; Kim, H.; Shin, S. Energy and Hydrodynamic Analyses of Coalescence-Induced Jumping Droplets. *Appl. Phys. Lett.* **2013**, *103*, 161601.
45. Peng, B. L.; Wang, S. F.; Lan, Z.; Xu, W.; Wen, R. F.; Ma, X. H. Analysis of Droplet Jumping Phenomenon with Lattice Boltzmann Simulation of Droplet Coalescence. *Appl. Phys. Lett.* **2013**, *102*, 151601.
46. He, M.; Zhang, Q. L.; Zeng, X. P.; Cui, D. P.; Chen, J.; Li, H. L.; Wang, J. J.; Song, Y. L. Hierarchical Porous Surface for Efficiently Controlling Microdroplets' Self-Removal. *Adv. Mater.* **2013**, *25*, 2291–2295.
47. Wisdom, K. M.; Watson, J. A.; Qua, X.; Liua, F.; Watson, G. S.; Chen, C. H. Self-Cleaning of Superhydrophobic Surfaces by Self-Propelled Jumping Condensate. *Proc. Natl. Acad. Sci. U.S.A.* **2013**, *110*, 7992–7997.
48. Miljkovic, N.; Enright, R.; Nam, Y.; Lopez, K.; Dou, N.; Sack, J.; Wang, E. N. Jumping-Droplet-Enhanced Condensation on Scalable Superhydrophobic Nanostructured Surfaces. *Nano Lett.* **2013**, *13*, 179–187.
49. Enright, R.; Miljkovic, N.; Al-Obeidi, A.; Thompson, C. V.; Wang, E. N. Superhydrophobic Condensation: The Role of Length Scale and Energy Barriers. *Langmuir* **2012**, *40*, 14424–14432.
50. Torresin, D.; Tiwari, M. K.; Del Col, D.; Poulikakos, D. Flow Condensation on Copper-Based Nanotextured Superhydrophobic Surfaces. *Langmuir* **2013**, *29*, 840–848.
51. Cheng, J.; Vandadi, A.; Chen, C. L. Condensation Heat Transfer on Two-Tier Superhydrophobic Surfaces. *Appl. Phys. Lett.* **2012**, *101*, 131909.
52. Azimi, G.; Dhiman, R.; Kwon, H. K.; Paxson, A. T.; Varanasi, K. K. Hydrophobicity of Rare-Earth Oxide Ceramics. *Nat. Mater.* **2013**, *12*, 315–320.
53. Torresin, D.; Tiwari, M. K.; Del Col, D.; Poulikakos, D. Flow Condensation on Copper-Based Nanotextured Superhydrophobic Surfaces. *Langmuir* **2013**, *29*, 840–848.
54. Lee, S.; Cheng, K.; Palmre, V.; Bhuiya, M. H.; Kim, K. J.; Zhang, B. J.; Yoon, H. Heat Transfer Measurement during Dropwise Condensation Using Micro/Nano-Scale Porous Surface. *Int. J. Heat Mass Transfer* **2013**, *65*, 619–626.
55. Boreyko, J. B.; Zhao, Y. J.; Chen, C. H. Planar Jumping-Drop Thermal Diodes. *Appl. Phys. Lett.* **2011**, *99*, 234105.
56. Boreyko, J. B.; Chen, C. H. Vapor Chambers with Jumping-Drop Liquid Return from Superhydrophobic Condensers. *Int. J. Heat Mass Transfer* **2013**, *61*, 409–418.
57. Boreyko, J. B.; Collier, P. C. Delayed Frost Growth on Jumping-Drop Superhydrophobic Surfaces. *ACS Nano* **2013**, *7*, 1618–1627.
58. Jung, S.; Tiwari, M. K.; Doan, N. V.; Poulikakos, D. Mechanism of Supercooled Droplet Freezing on Surfaces. *Nat. Commun.* **2012**, *3*, 615.
59. Miljkovic, N.; Enright, R.; Wang, E. N. Liquid Freezing Dynamics on Hydrophobic and Superhydrophobic Surfaces. *J. Heat Transfer* **2012**, *134*, 080902.

60. Cao, L. L.; Jones, A. K.; Sikka, V. K.; Wu, J. Z.; Gao, D. Anti-Icing Superhydrophobic Coatings. *Langmuir* **2009**, *25*, 12444–12448.
61. Kim, P.; Wong, T. S.; Alvarenga, J.; Kreder, M. J.; Adorno-Martinez, W. E.; Aizenberg, J. Liquid-Infused Nanostructured Surfaces with Extreme Anti-Ice and Anti-Frost Performance. *ACS Nano* **2012**, *6*, 6569–6577.
62. Meuler, A. J.; McKinley, G. H.; Cohen, R. E. Exploiting Topographical Texture To Impart Icephobicity. *ACS Nano* **2010**, *4*, 7048–7052.
63. Zhang, Q.; He, M.; Chen, J.; Wang, J.; Song, Y.; Jianga, L. Anti-Icing Surfaces Based on Enhanced Self-Propelled Jumping of Condensed Water Microdroplets. *Chem. Commun.* **2013**, *49*, 4516–4518.
64. Chen, X.; Ma, R.; Zhou, H.; Zhou, X.; Che, L.; Yao, S.; Wang, Z. Activating the Microscale Edge Effect in a Hierarchical Surface for Frosting Suppression and Defrosting Promotion. *Sci. Rep.* **2013**, *3*, 2515.
65. Miljkovic, N.; Enright, R.; Wang, E. N. Growth Dynamics during Dropwise Condensation on Nanostructured Superhydrophobic Surfaces. *3rd Micro/Nanoscale Heat Mass Transf. Int. Conference*; American Society of Mechanical Engineers (ASME): Atlanta, GA, USA, **2012**.
66. Miljkovic, N.; Enright, R.; Wang, E. N. Modeling and Optimization of Superhydrophobic Condensation. *J. Heat Transfer* **2013**, *135*, 111004.
67. Miljkovic, N.; Preston, D. J.; Enright, R.; Wang, E. N. Electrostatic Charging of Jumping Droplets. *Nat. Commun.* **2013**, *4*, 2517.
68. Stone, H. A. Dynamics of Drop Deformation and Breakup in Viscous Fluids. *Annu. Rev. Fluid Mech.* **1994**, *26*, 65–102.
69. White, F. M. *Fluid Mechanics*, 6th ed.; McGraw-Hill: New York, 2008; p xiii.
70. Paulsen, J. D.; Burton, J. C.; Nagel, S. R.; Appathurai, S.; Harris, M. T.; Basaran, O. A. The Inexorable Resistance of Inertia Determines the Initial Regime of Drop Coalescence. *Proc. Natl. Acad. Sci. U.S.A.* **2012**, *109*, 6857–6861.
71. Eggers, J.; Lister, J. R.; Stone, H. A. Coalescence of Liquid Drops. *J. Fluid Mech.* **1999**, *401*, 293–310.
72. Paulsen, J. D.; Burton, J. C.; Nagel, S. R. Viscous to Inertial Crossover in Liquid Drop Coalescence. *Phys. Rev. Lett.* **2011**, *106*, 114501.
73. Wu, M. M.; Cubaud, T.; Ho, C. M. Scaling Law in Liquid Drop Coalescence Driven by Surface Tension. *Phys. Fluids* **2004**, *16*, 51–54.
74. Enright, R.; Miljkovic, N.; Sprittles, J.; Mitchell, R.; Nolan, K.; Thompson, C. V.; Wang, E. N. Energy Transfer during Inertial-Capillary-Driven Droplet Jumping on Superhydrophobic Surfaces. In review.
75. Carey, V. P. *Liquid-Vapor Phase-Change Phenomena: An Introduction to the Thermophysics of Vaporization and Condensation Processes in Heat Transfer Equipment*, 2nd ed.; Taylor and Francis: New York, 2008; p xxii.
76. Chang, T. B. Mixed-Convection Film Condensation along Outside Surface of Vertical Tube in Saturated Vapor with Forced Flow. *Appl. Therm. Eng.* **2008**, *28*, 547–555.
77. Michael, A. G.; Rose, J. W.; Daniels, L. C. Forced Convection Condensation on a Horizontal Tube-Experiments with Vertical Downflow of Steam. *J. Heat Transfer* **1989**, *111*, 792–797.
78. Zhang, L.; Subramanian, R. S.; Balasubramanian, R. Motion of a Drop in a Vertical Temperature Gradient at Small Marangoni Number - The Critical Role of Inertia. *J. Fluid Mech.* **2001**, *448*, 197–211.
79. Rose, J. W.; Glicksman, L. R. Dropwise Condensation - The Distribution of Drop Sizes. *Int. J. Heat Mass Transfer* **1973**, *16*, 411–425.
80. Kundu, P. K.; Cohen, I. M.; Dowling, D. R. *Fluid Mechanics*, 5th ed.; Academic Press: Waltham, MA, 2012; p xxvi.
81. Lee, S. J.; Lee, S.; Kang, K. H. Jumping of a Droplet on a Superhydrophobic Surface in AC Electrowetting. *J. Visual.-Japan* **2011**, *14*, 259–264.
82. Xiao, R.; Wang, E. N. Microscale Liquid Dynamics and the Effect on Macroscale Propagation in Pillar Arrays. *Langmuir* **2011**, *27*, 10360–10364.
83. Xiao, R.; Enright, R.; Wang, E. N. Prediction and Optimization of Liquid Propagation in Micropillar Arrays. *Langmuir* **2010**, *26*, 15070–15075.
84. Peters, T. B.; McCarthy, M.; Allison, J.; Dominguez-Espinosa, F. A.; Jenicek, D.; Kariya, H. A.; Staats, W. L.; Brisson, J. G.; Lang, J. H.; Wang, E. N. Design of an Integrated Loop Heat Pipe Air-Cooled Heat Exchanger for High Performance Electronics. *IEEE Trans. Compon., Packag. Manuf.* **2012**, *2*, 1637–1648.
85. Faghri, A. *Heat Pipe Science and Technology*, 2nd ed.; Global Digital Press: Columbia, MO, 2010.
86. Nam, Y.; Sungtaek, Y. A Comparative Study of the Morphology and Wetting Characteristics of Micro/Nanostructured Cu Surfaces for Phase Change Heat Transfer Applications. *J. Adhes. Sci. Technol.* **2012**, *27*, 2163–2176.

# Supplementary Information

## Electric-Field-Enhanced Condensation on Superhydrophobic Nanostructured Surfaces

Nenad Miljkovic,<sup>1</sup> Daniel J. Preston,<sup>1</sup> Ryan Enright,<sup>2,§</sup> and Evelyn N. Wang<sup>1,\*</sup>

<sup>1</sup>*Department of Mechanical Engineering, Massachusetts Institute of Technology,  
77 Massachusetts Avenue, Cambridge, Massachusetts 02139, USA*

<sup>2</sup>*Thermal Management Research Group, Efficient Energy Transfer ( $\eta$ ET) Department, Bell Labs Ireland, Alcatel-Lucent Ireland Ltd., Blanchardstown Business & Technology Park, Snugborough Rd, Dublin 15, Ireland*

<sup>§</sup>Work initiated while affiliated with <sup>1</sup> and Stokes Institute, University of Limerick, Limerick, Ireland

\*Address correspondence to [enwang@mit.edu](mailto:enwang@mit.edu)

### S1. HIGH SPEED MOVIES

**Movie 1.** Jumping droplet return, multi-coalescence, and jumping captured with a high speed camera (Phantom v7.1, Vision Research). The sample surface was a flat 3 cm x 3 cm CuO-nanostructured Cu substrate coated with TFTS (shown on the bottom of the video facing upwards). The sample surface was horizontally oriented (gravity facing downwards). A small ( $R \approx 16.6 \pm 4.1 \mu\text{m}$ ) droplet initially jumped upwards from the surface and decelerated due to gravity, reversed direction and travelled back down towards the surface. Once the droplet returned to the surface, it coalesced with another droplet on the surface and underwent a second jump. The vapor pressure was  $\approx 2.7$  kPa. The video was captured at 2900 fps and is played back at 20 fps. The field of view is 3.3 mm x 2.5 mm.

**Movie 2.** Jumping droplet return and pinning captured with a high speed camera (Phantom v7.1, Vision Research). The sample surface was a flat 3 cm x 3 cm CuO-nanostructured Cu substrate coated with TFTS (shown on the bottom of the video facing upwards). The sample surface was horizontally oriented (gravity facing downwards). A small ( $R \approx 25 \pm 4.1 \mu\text{m}$ ) droplet initially jumped upwards from the surface and decelerated by gravity, reversed direction and travelled back down towards the surface. Once the droplet returned to the surface, it remained on the surface (due to contact line pinning) and continued to grow until jumping occurred again. The vapor pressure was  $\approx 2.7$  kPa. The video was captured at 2900 fps and is played back at 20 fps. The field of view is 3.3 mm x 2.5 mm.

**Movie 3.** Steady state condensation on the nanostructured CuO tube captured with a high speed camera (Phantom v7.1, Vision Research). The tube was oriented in the horizontal direction with cooled water flowing inside the tube at  $5 \pm 0.25$  L/min. The vapor pressure was  $\approx 2.7$  kPa and  $\Delta T_{\text{LMTD}} \approx 1$  K. Droplet removal *via* coalescence-induced ejection occurred once droplets reached sizes large enough to begin coalescing. The video was captured at 200 fps and is played back at 20 fps. The field of view is 16.0 mm x 12.0 mm.

**Movie 4.** Steady state condensation on the nanostructured CuO tube with a flow blockage beneath the tube captured with a high speed camera (Phantom v7.1, Vision Research). The flow blockage was installed to test whether droplet jumping and return against gravity was due to bulk vapor flow upwards past the tube (due to buoyancy). The tube

was oriented in the horizontal direction with cooling water flowing inside the tube at  $5 \pm 0.25$  L/min. The vapor pressure was  $\approx 2.7$  kPa and  $\Delta T_{\text{LMTD}} \approx 1$  K. Droplet removal *via* coalescence-induced ejection occurred once droplets reached sizes large enough to begin coalescing. The video was captured at 200 fps and is played back at 20 fps. The field of view is 15.0 mm x 11.3 mm.

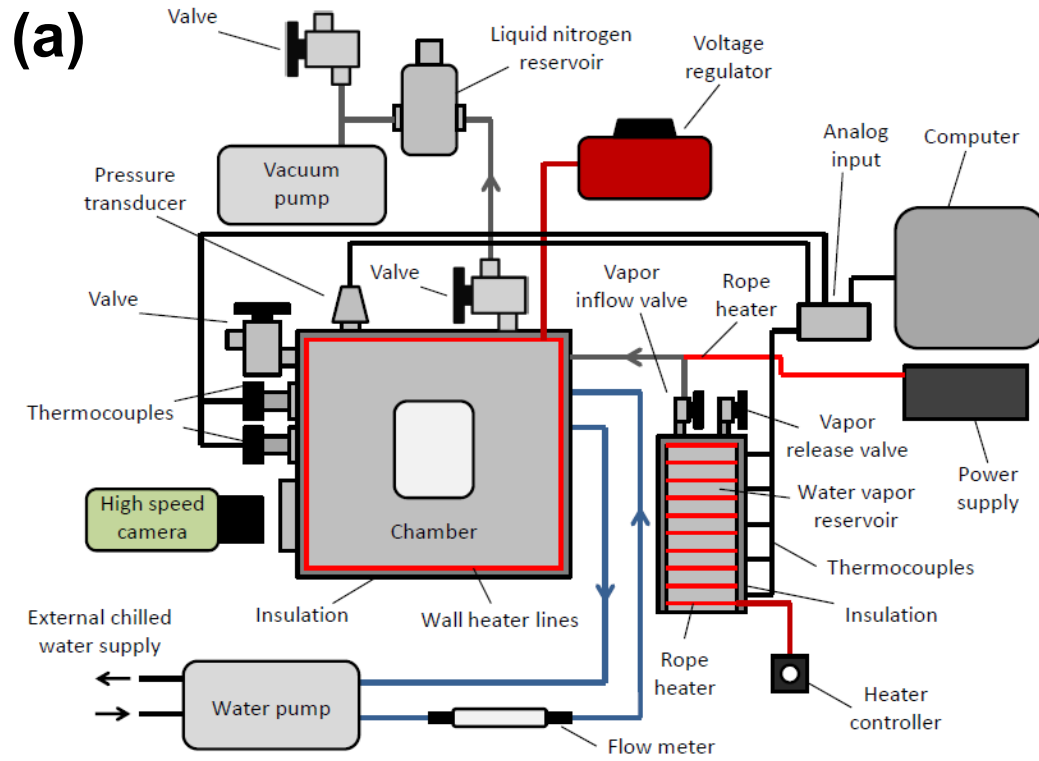
## S.2 CONDENSATION CHAMBER SETUP

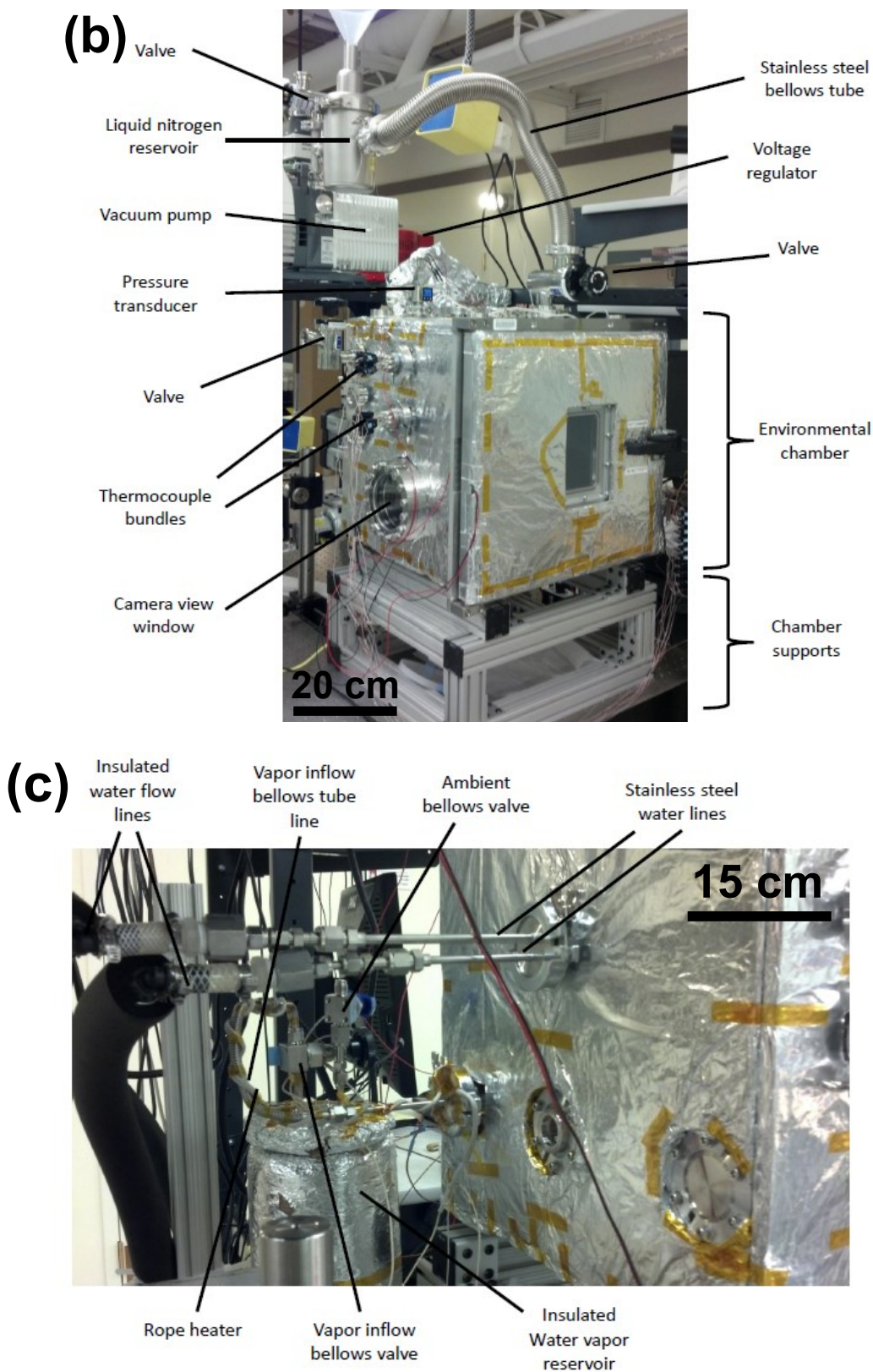
The custom environmental chamber used for this work (Kurt J. Lesker) consists of a stainless steel frame with a door (sealed with a rubber gasket), two viewing windows, and apertures for various components. Resistive heater lines were wrapped around the exterior of the chamber walls to prevent condensation at the inside walls and then insulated on the exterior walls. The output power of the resistive heater lines was controlled by a voltage regulator (Variac). Two insulated stainless steel water flow lines (Swagelok) were fed into the chamber *via* a KF flange port (Kurt J. Lesker) to supply cooling water to the chamber from a large capacity chiller (System III, Neslab). The cooling water flow rate was measured *via* an in-line liquid flow meter (0-5 L/min L-Series liquid flow meter, Alicat)

A secondary stainless steel tube line was fed into the chamber *via* a KF adapter port that served as the flow line for the incoming water vapor supplied from a heated steel water reservoir. The vapor line was wrapped with a rope heater (60 W, Omega) and controlled by a power supply (Agilent). The vapor reservoir was wrapped with another independently-controlled rope heater (120 W, Omega) and insulated to limit heat losses to the environment. The access tubes were welded to the vapor reservoir, each with independently-controlled valves. The first valve (Diaphragm Type, Swagelok), connecting the bottom of the reservoir to the ambient, was used to fill the reservoir with water. The second valve (BK-60, Swagelok), connecting the top of the reservoir to the inside of the chamber, provided a path for vapor inflow. K-type thermocouples were located along the length of the water vapor reservoir to monitor temperature.

A bellows valve (Kurt J. Lesker) was attached to the chamber to serve as a leak port between the ambient and inside of the chamber. In order to monitor temperatures within the chamber, K-type thermocouple bundles were connected through the chamber apertures *via* a thermocouple feed through (Kurt J. Lesker). To provide electrical connections inside the chamber for LED lighting and electric field generation, insulated copper electrical wires were connected through the chamber apertures *via* an electrical feed through (Kurt J. Lesker). A pressure transducer (925 Micro Pirani, MKS) was attached to monitor pressure within the chamber. The thermocouple bundles and the pressure transducer were both electrically connected to an analog input source (DAQ DAQ, National Instruments), which was interfaced to a computer for data recording. A second bellows valve (Kurt J. Lesker) was integrated onto the chamber for the vacuum pump, which brought down the chamber to vacuum conditions prior to vapor filling. A liquid nitrogen cold trap was incorporated along the line from the chamber to the vacuum which served to remove any moisture from the pump-down process and ultimately assist in yielding higher quality vacuum conditions. A tertiary bellows valve (Kurt J. Lesker) was integrated on a T fitting between the vacuum pump and liquid nitrogen reservoir to connect the vacuum line to the ambient to release the vacuum line to ambient conditions once pump down was achieved. In order to visually record data, a high speed camera (Phantom v7.1, Vision Research) was

placed in line with the 5" viewing windows on the chamber. In addition, a digital SLR camera (Cannon) was interchangeable with the high speed camera to obtain color images. The schematic of the exterior of the environmental setup is depicted in Figure S1a. Images of the front and rear of the experimental setup are shown in Figures S1b and c, respectively.

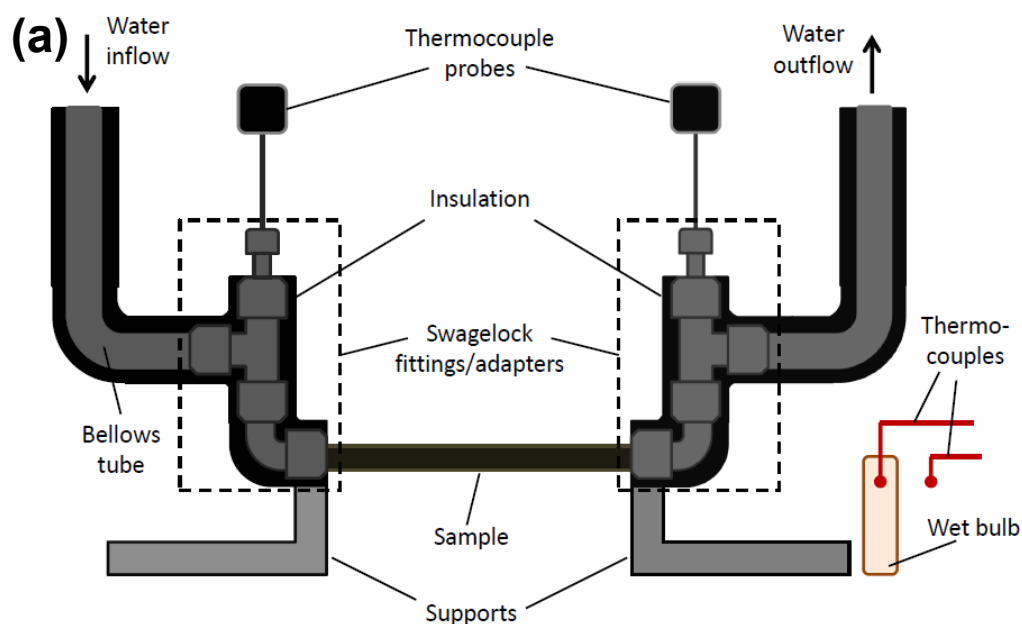




**Figure S1.** (a) Schematic of experimental setup (not to scale). (b) Image of the experimental setup shown from the front (high speed camera and data acquisition system not shown). (c) Image of the experimental setup from the rear of the chamber showing the cooling water inlet and outlet and water vapor reservoir.

The setup used to run experiments inside the chamber is shown in Figure S2. Stainless steel bellows tube lines (1/4", Swagelok) were connected to the external water flow lines (Figure S1c). T-connection adapters (Swagelok) with bore through Ultra-Torr fittings (Swagelok) were used to adapt K-type thermocouple probes (Omega) at the water inlet and outlet.

The CuO nanostructure test sample consisted of a 6.35 mm diameter tube, which was connected *via* a Swagelok compression fitting onto the T-connection. Chilled water flows through the inlet bellows tube, along the inside of the tube sample and through the outlet. Two supports were used to hold the sample and the entire configuration in place. Two separate pieces of insulation were embedded with K-type thermocouple leads and used for wet bulb temperature measurement during experimental runs. A third thermocouple was placed beside the sample to measure the reference temperature inside the chamber.



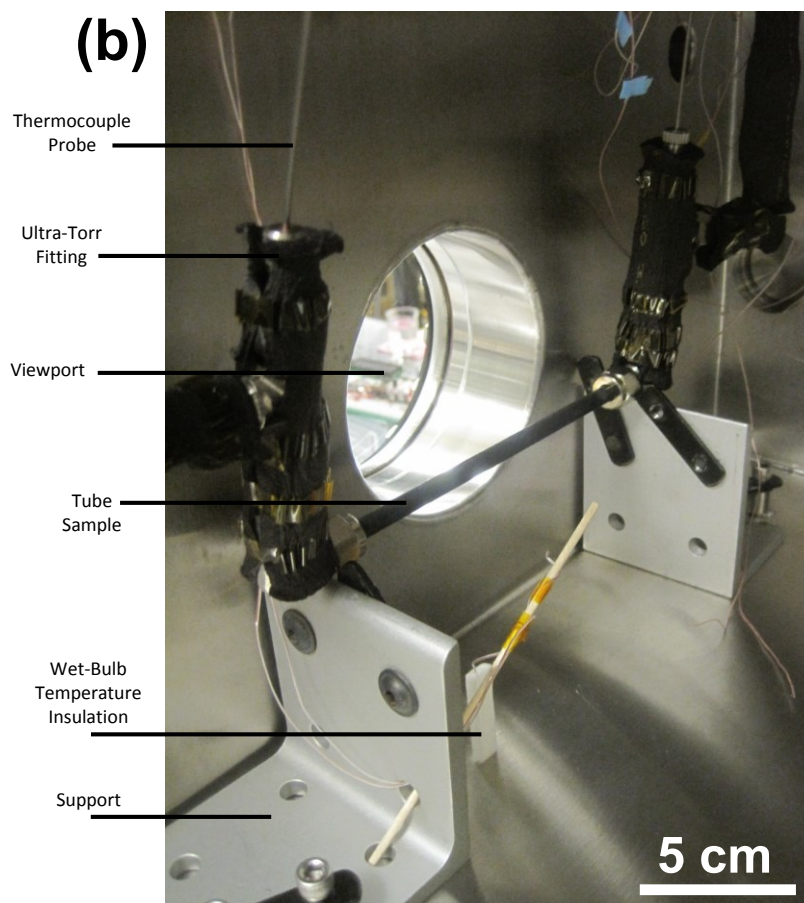


**Figure S2.** (a) Schematic of experimental setup inside the chamber (not to scale). (b) Image of the experimental setup inside the chamber showing a CuO nanostructured tube in place for testing.

### S.3 CONDENSATION PROCEDURE

For each experimental run, a set of strict procedures were followed to ensure consistency throughout the experiments. The first step of the process was to turn on the voltage regulator to heat up the environmental chamber walls, which prevented condensation on the chamber walls. Simultaneously, the water vapor reservoir was filled with approximately 3.5 liters of DI water (99% full) using a syringe through the vapor release valve. After opening the vapor inflow valve and closing the vapor release valve, the rope heater around the water vapor reservoir was turned on with the heater controller set to maximum output (120 W). Then the rope heater connected to the vapor inflow valve was turned on. The temperature of the water reservoir was monitored with the installed thermocouples; the temperature at the top of the reservoir was higher than that of the middle/bottom of the reservoir due to the water thermal-mass present at the middle/bottom section. Hence, we ensured that the regions of the water reservoir of higher thermal capacity were brought to a sufficiently high temperature for boiling. During the boiling process, aluminum foil was placed on the bottom surface of the inner chamber to collect any of the water leaving the vapor inflow line. Once boiling was achieved and all thermocouples on the reservoir were  $>95^{\circ}\text{C}$  for at least 10 minutes, the vapor inflow valve was closed. The excess water that spilled inside the chamber during de-gassing of the reservoir was removed.

To install the samples onto the rig (Figure S2), the Swagelok female adapters at the ends of the tube samples were connected to the 90 degree male elbow connectors on the rig. Before installing the entire sample setup in the chamber, all adapters/connecters were tightened to ensure that there were no leaks that could affect vacuum performance. The setup was then placed on top of the steel supports and the bellows tubes (for the water inflow/outflow) were connected to the water lines. Then the insulating wet bulb wick was placed near the sample and in contact with the bottom surface of the chamber.

The next step was to begin the vacuum pump-down procedure. Initially, the liquid nitrogen cold trap was filled to about half capacity. The ambient exposed valves connecting the chamber and the vacuum pump were both closed and the valve connected to the liquid nitrogen cold trap was opened. The vacuum pump was then turned on, initiating the pump-down process. The pressure inside the chamber was monitored during the pump-down process. This process took approximately one hour in order to achieve the target vacuum conditions ( $0.5 \text{ Pa} < P < 1 \text{ Pa}$ ). The experimental operating pressure of non-condensable was set to be a maximum of 0.25% of the operating pressure. Non-condensable gas content of above 0.5% (pressure) was shown to significantly degrade performance during dropwise condensation.<sup>1, 2</sup> In our experiments, extreme care was taken to properly de-gas the vacuum chamber and water vapor reservoir prior to experimental testing. In addition, the chamber leak rate was characterized prior to each run in order to estimate the maximum time available for acquiring high fidelity data with non-condensable content of less than 0.25%.

The setup of the water flow-loop is described as follows. The Neslab water pump reservoir was filled and turned on to a flow rate of  $0.5 \pm 0.025 \text{ L/min}$  (for heat transfer measurement experiments). The flow rate was monitored with the flow meter integrated in the inflow water line (0-5 L/min L-Series liquid flow meter, Alicat). In order to bring the chilled water into the flow loop and to the tube sample, the external chilled water lines were opened.

Prior to beginning experiments, the high-speed camera was turned on for visual recording of the sample during condensation. Afterwards, the rope heater around the water reservoir was turned off and the vapor inflow valve was slowly turned open until the operating pressure was reached. Steady state conditions were typically reached after 2 minutes of full operation.

#### **S.4 BULK VAPOR FLOW**

Bulk vapor flow from buoyancy effects in the surrounding vapor can lead to vapor return. To prevent vapor from condensing on the chamber walls during testing, the temperature of the chamber during condensation testing was superheated ( $\Delta T = T_{\text{wall}} - T_{\text{sat}} \approx 4^\circ\text{C}$ ). The higher temperature of the bottom chamber wall could create a buoyant vapor flow upwards past the tube which would entrain departing droplets. To test the bulk vapor flow hypothesis, we modified the experimental setup to include a blockage beneath the tube such that any bulk vapor flow would be diverted past the sides of the tube and not interfere with droplet jumping (Figure S3). Test results after installation of the blockage showed no change in jumping droplet behavior. Return of droplets from the bottom surface was as

frequent as prior to installation of the blockage (see Supplementary Movie 4). The results indicated that droplet entrainment in a bulk vapor flow was not the mechanism of droplet return against gravity.

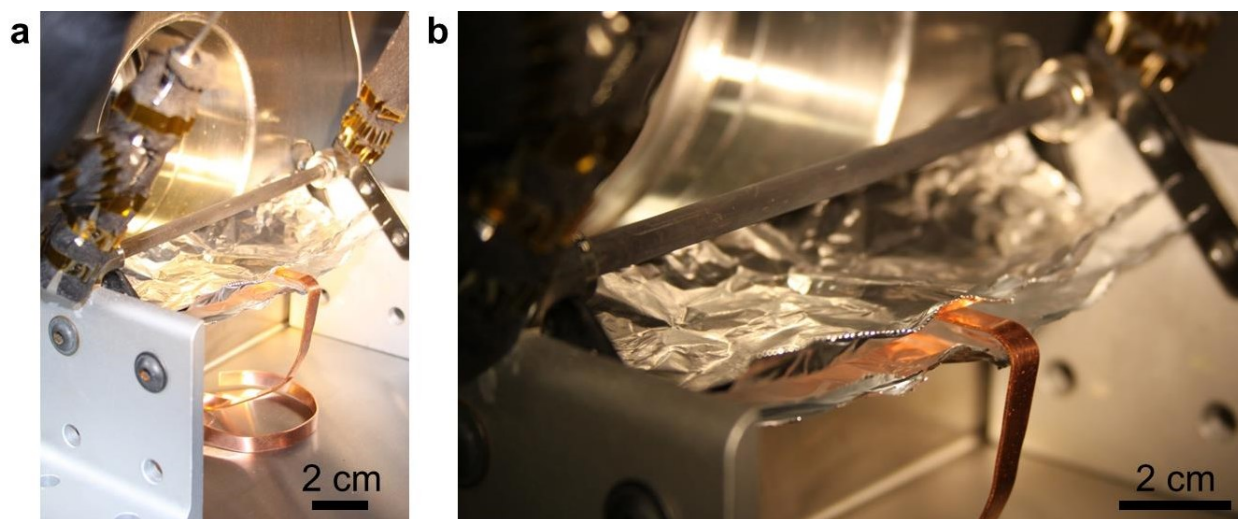


**Figure S3. Effect of bulk vapor flow on jumping droplet return.** Images of the experimental setup with a blockade placed beneath the condensing surface consisting of an aluminum foil sheet used to divert any bulk vapor flow upwards past the tube and limit interference with droplets traveling downwards.

## S.5 JUMPING DROPLET INITIAL VELOCITY

The droplet ejection process was captured under saturated conditions inside the environmental chamber (Section S2) using a single-camera setup.<sup>3</sup> The out-of-plane trajectory of the ejected droplets was captured using a high-speed camera (Phantom v7.1, Vision Research) at frame rates of 7200, 10000 and 20000 fps corresponding to shutter speeds of 139  $\mu$ s, 100  $\mu$ s and 50  $\mu$ s, respectively. The camera was mounted outside the environmental chamber and fitted with an extended macro lens assembly (Figure S4). The lens assembly consisted of a fully extended 5X optical zoom macro lens (MP-E 65 mm, Canon), connected in series with 3 separate 68 mm extension tubes (Auto Extension Tube Set DG, Kenko). The DG extension tubes enable the lens to focus closer than its normal set minimum focal distance, which has the effect of magnifying the image (making it appear larger in the viewfinder). The DG extension tubes have no optics. They were mounted in between the camera body and lens to create more distance between the lens and film plane. By moving the lens further away from the film or CCD sensor in the camera, the lens was allowed to focus much closer than normal. Illumination was supplied by light emitting diodes installed inside the chamber and providing back lighting to the sample.

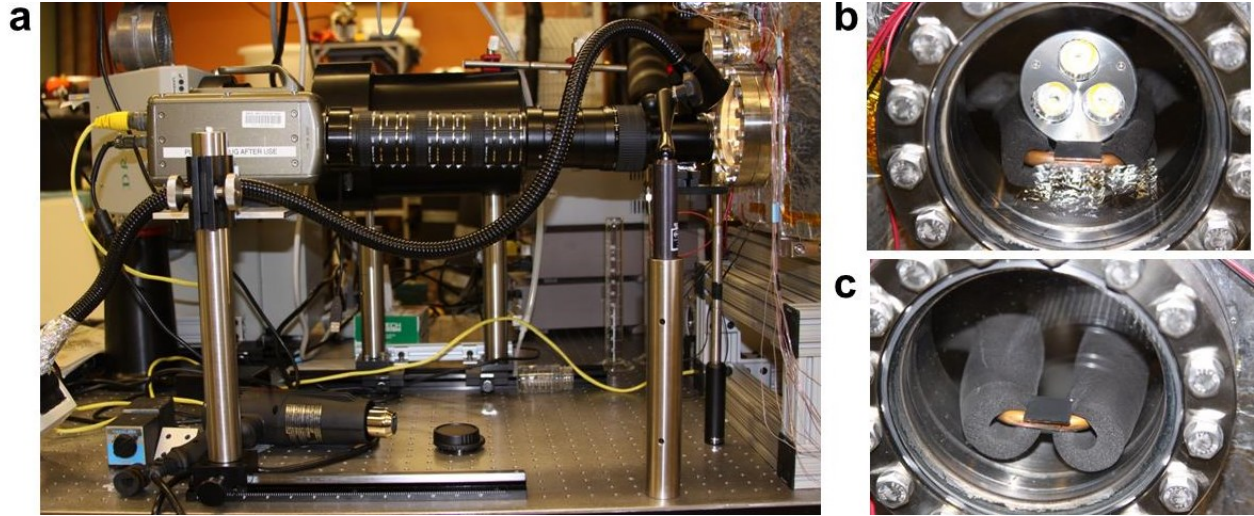


**Figure S4. High speed and high magnification imaging setup for jumping droplets.** Images of the (a) experimental setup showing the high speed camera placed adjacent to the chamber and retrofitted with extension tubes for higher magnification imaging. Images showing the sample holder inside the chamber (b) with LED light placed behind and (c) without LED light.

The experiment was initiated by first evacuating the environmental chamber to medium-vacuum levels ( $=0.5 \pm 0.025$  Pa, see section S3). The sample was mounted to a flattened copper tube connected to an external cooling loop and was maintained at a temperature of  $T_w = 26$  °C ( $p_w = 3.33$  kPa) (Figure S4b,c). The water vapor supply was vigorously boiled before the experiments to remove non-condensable gases. Water vapor was introduced into the environmental chamber *via* a metering valve set to maintain the chamber pressure at  $p_v = 3.6 \pm 0.175$  kPa. Figure S5 shows a typical high speed time-lapse obtained during jumping-droplet condensation.

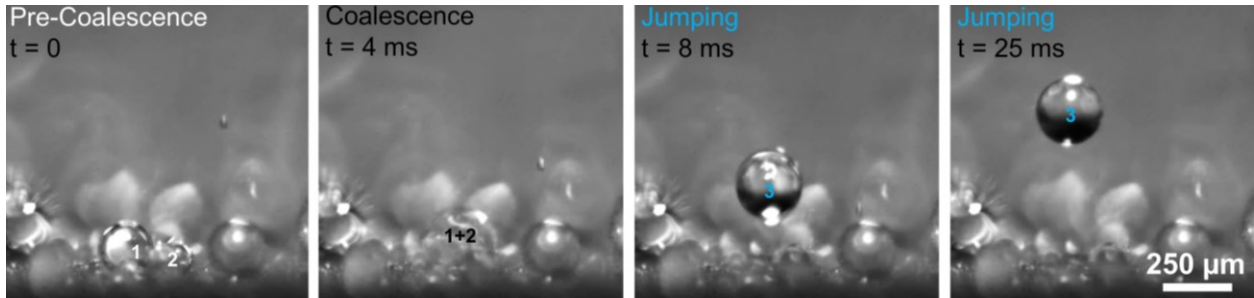


**Figure S5. High speed droplet jumping images.** Time-lapse images captured *via* high speed camera (Figure S4) of water condensation on the nanostructured CuO surface. Droplet 1 and 2 initially grow independently until coalescing and then jumping from the surface ( $P_v = 3600 \pm 175$  Pa,  $T_s = 26 \pm 0.2$  °C).

The initial droplet ejection velocity ( $U$ ) as a function of droplet diameter ( $2R$ ) is shown in Figure S6. The experimental results show good agreement with the inertial-capillary scaling by balancing the surface energy and kinetic energy of the ejected droplet to obtain a characteristic ejection velocity of

$$U \sim \sqrt{\gamma/\rho R}. \quad (\text{S1})$$

This characteristic velocity corresponds to a value of unity for the Weber number,  $We = \rho_w U^2 R / \gamma = 1$ , where  $\gamma$  is the water surface tension ( $\approx 72$  mN/m). In order to account for the incomplete conversion of excess surface energy to kinetic energy not captured by the scaling, we introduced a proportionality constant  $C$ , on the right hand side of equation (S1).<sup>4</sup> For our experiments on CuO at low vapor pressure ( $P_v < 4000$  Pa), equation (S1) best fits the experimental data with  $C \approx 0.23$ .

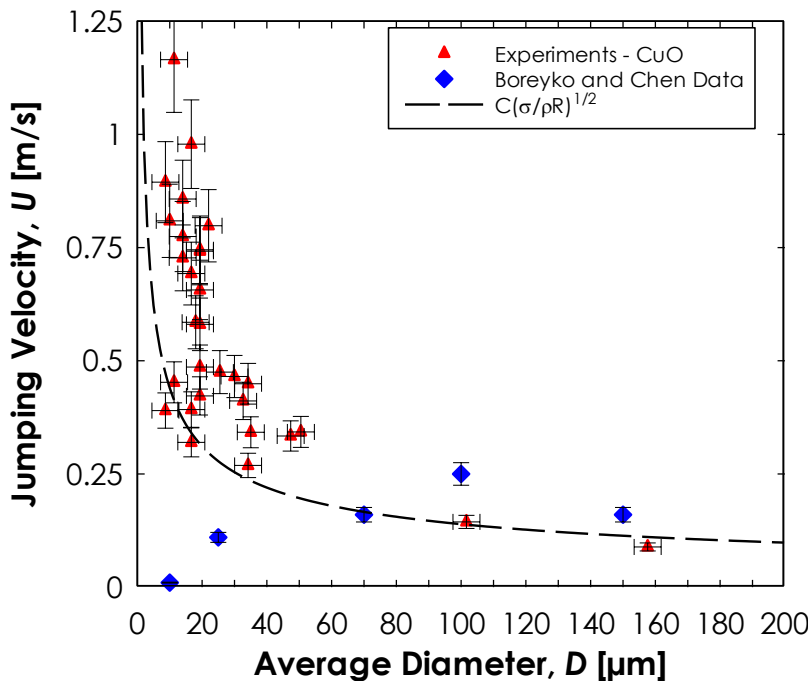


**Figure S6. Droplet size dependence on jumping droplet initial velocity.** Experimentally determined initial jumping droplet velocity ( $U$ ) as a function of droplet diameter ( $2R$ ). Results show good agreement with inertial-capillary scaling with a prefactor of  $C \approx 0.23$ .

## S.6 DROPLET INTERACTION WITH AN ELECTRIC FIELD

To demonstrate droplet interaction with an external electric field, the experimental setup was modified to include an electrode placed beneath the CuO nanostructured tube (Figure S7). The electrode (red insulated wire) was connected to the insulated copper electrical feed through and brought in close proximity ( $< 1$  cm) to the tube *via* an insulated copper holder made from a strip of copper sheet. To electrically insulate the holder, a piece of insulation was placed beneath it (Figure S7a). The electrode was energized by an external 600 V DC power supply (N5752A, Agilent Technologies). The negative terminal of the power supply was grounded to the tube. The terminals could be reversed externally in order to study the polarity of the droplet charge by reversing the direction of the established electric field between the electrode and grounded tube. Figure S7c and d show typical views from the side viewport of the tube-electrode setup before and after condensation initiates ( $\Delta V = 0$  V), respectively. To monitor the local temperature close to the electrode, a K-type thermocouple was placed in close proximity (Figure S7c and d).

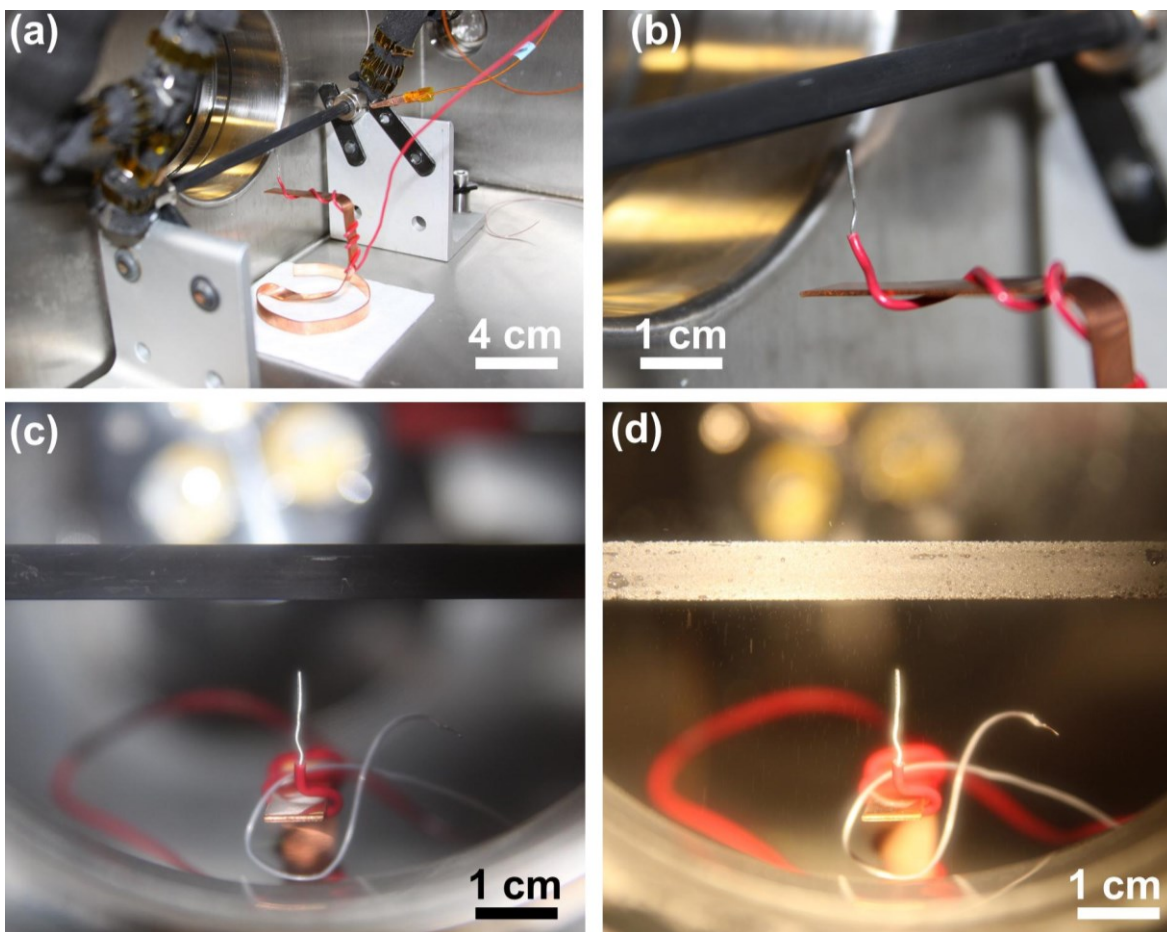


**Figure S7** – (a) Image of the electrode experimental setup inside the chamber. The red wire is connected to the external DC power supply *via* a feed through to the right (not seen). (b) Close-up image of the electrode beneath the CuO nanostructured tube sample. Electrical bias between the electrode and tube created an electrostatic field which could manipulate charged droplets to move towards or away from the electrode. Image of the electrode and tube from the front view port (c) prior to condensation, and (d) after condensation initiated ( $\Delta V = 0$  V,  $P_v = 2700 \pm 70$  Pa,  $S \approx 1.04$ ).

## S.7 FLOODING MECHANISMS

Jumping-droplet condensation has two distinct flooding mechanisms: nucleation-density-mediated flooding,<sup>5-7</sup> and progressive flooding (Figure S8). Nucleation-density-mediated flooding can be explained in terms of the interplay between the characteristic structure length scale and droplet nucleation density.<sup>5</sup> At low supersaturations ( $S < 1.12$ , low nucleation density), droplets form with large spacings between each other relative to the spacing of the CuO nanostructures such that droplets could evolve into the energetically favorable partially wetting (PW) Cassie-like morphology.<sup>8</sup> For higher supersaturations ( $S > 1.12$ ), the droplet nucleation density increases to the point where droplet/droplet interactions occur on a similar length scale as the nanostructure spacing ( $\approx 1$   $\mu\text{m}$ ), and droplets, instead of forming in the energetically favorable PW morphology, merge to form pinned liquid films due to contact line depinning at their base. Further condensation on the “flooded” surface results in the formation of Wenzel droplets which demonstrate significant contact line pinning, large droplet shedding diameters, and irregular droplet shapes (Figure S8a).

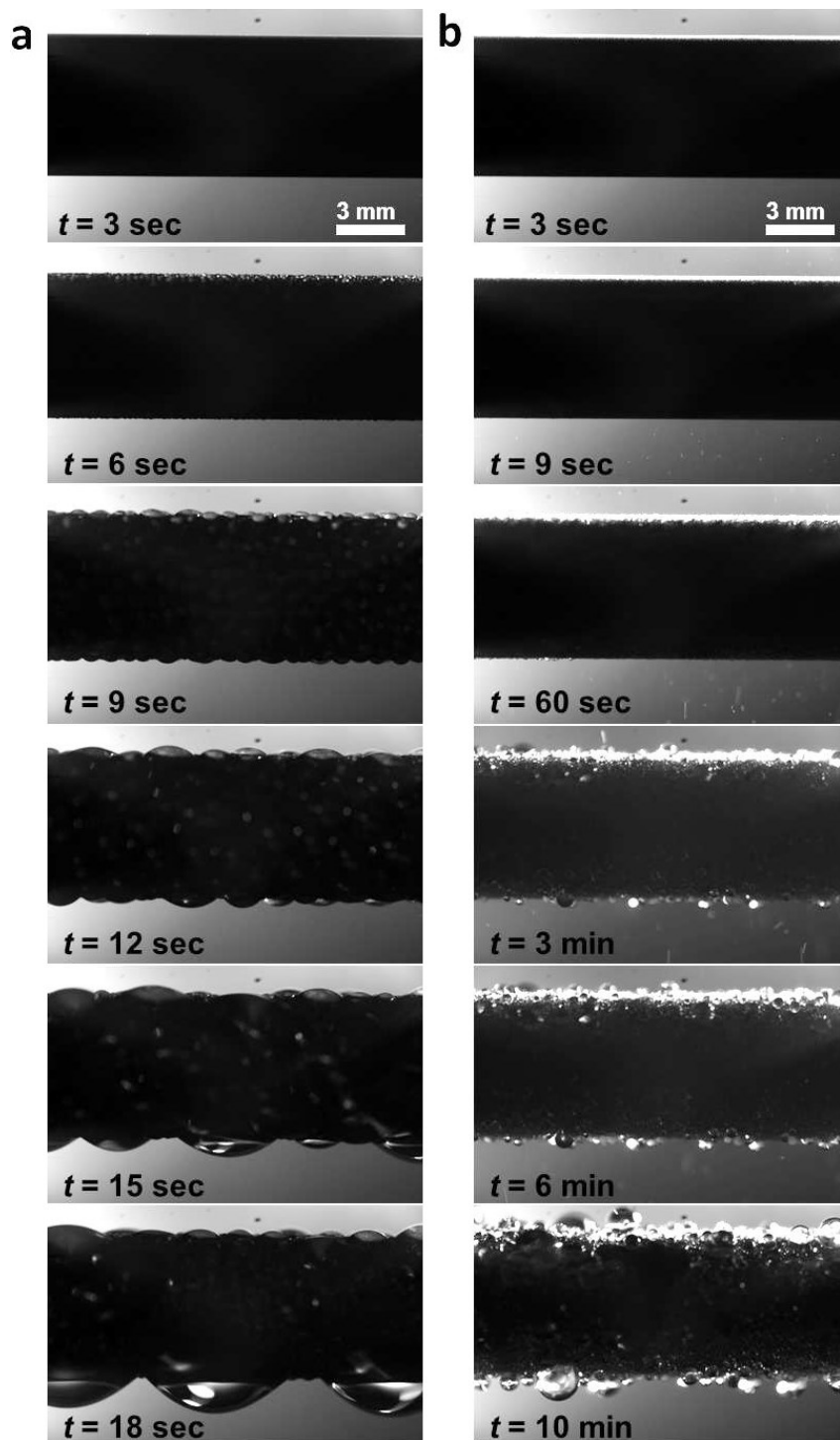


**Figure S8** - Time-lapse images of (a) nucleation-density-mediated flooding ( $P_v = 2700 \pm 75$  Pa,  $S \approx 1.5$ ) and (b) progressive flooding ( $P_v = 2700 \pm 75$  Pa,  $S \approx 1.08$ ) on a superhydrophobic CuO surface. Jumping-droplet condensation with progressive flooding shows significant droplet return to the surface due to vapor flow entrainment. As droplets return, some may coalesce and jump again (see Supplementary Movie 1), while others may remain pinned to the surface (see Supplementary Movie 2). As time progressed ( $t \rightarrow 10$  min) the average droplet size on the surface increased and limited heat transfer performance. Nucleation-density-mediated flooding occurred very quickly ( $t < 18$  s) and resulted in no droplet jumping due to the formation of highly pinned Wenzel droplets.<sup>5-7</sup>

Progressive flooding occurs due to the return of vapor entrained jumping droplets back to the condensing surface. As droplets return, some may coalesce and jump again (see Supplementary Movie 1), while others may remain pinned to the surface (see Supplementary Movie 2). In contrast to nucleation-density-mediated flooding, the pinned droplets remain in a PW wetting (Cassie like) morphology and have the potential to can merge again with neighboring droplets and jump from the surface. Over time however, the ‘progressive’ return and pinning on droplets results in a higher population of large droplets (Figure S8b), and gradual degradation in heat transfer performance. Due to the relation between vapor velocity and condensation heat flux (supersaturation), lower supersaturations result in smaller degrees of progressive flooding on the condensing surface and slower degradation of performance over time.

It is important to note, the heat transfer values reported in Nano Letters<sup>7</sup> are still valid, but represent the peak limit to heat transfer during the no-field jumping-droplet condensation mode. Due to the lack of longevity studies, *i.e.*, >5 minutes, (which was outside of the scope of the initial Nano Letters paper), the progressive flooding phenomenon was not identified, and therefore, not reported.

## S.8 HEAT TRANSFER MODEL

For the model,  $h_c$  was obtained by incorporating the individual droplet heat transfer with droplet size distribution:<sup>8,9</sup>

$$h_c = \frac{q''}{\Delta T} = \frac{1}{\Delta T} \int_{R^*}^{R_c} q(R)n(R)dR, \quad (\text{S2})$$

$$q(R) = \frac{\pi R^2 \left( \Delta T - \frac{2T_{sat}\gamma}{Rh_{fg}\rho_w} \right)}{\frac{1}{2h_{int}(1 - \cos \theta)} + \frac{R\theta}{4k_w \sin \theta} + \frac{1}{k_{HC} \sin^2 \theta} \left[ \frac{k_p \varphi}{\delta_{HC} k_p + h k_{HC}} + \frac{k_w(1 - \varphi)}{\delta_{HC} k_w + h k_{HC}} \right]^{-1}}, \quad (\text{S3})$$

where  $q''$  steady state dropwise condensation heat transfer rate per unit area of the condensing surface,  $\Delta T$  is the temperature difference between the saturated vapor and sample outer surface ( $\Delta T = (T_{sat}(P) - T_s)$ ),  $R^*$  is the critical radius for heterogeneous nucleation ( $R^* = r_c$ ),<sup>10</sup>  $R_c$  is the droplet coalescence radius,  $q(R)$  is the individual droplet heat transfer (equation (S2)),  $n(R)$  is the non-interacting droplet size distribution,<sup>9</sup>  $R$  is the droplet radius,  $\gamma$  is the condensate surface tension,  $h_{fg}$  is the latent heat of phase change,  $\rho_w$  is the condensate density (liquid water),  $\theta$  is the droplet contact angle,  $h_{int}$  is the interfacial heat transfer coefficient,<sup>11</sup>  $k_w$  is the condensate thermal conductivity,  $k_{HC}$  is the hydrophobic coating thermal conductivity,  $\varphi$  is the structured surface solid fraction ( $\approx 0.023$ ),  $h$  is the structured surface height ( $\approx 1 \mu\text{m}$ ), and  $\delta_{HC}$  is the hydrophobic coating thickness ( $\approx 10 \text{ nm}$ ).<sup>6</sup>

The size distribution  $n(R)$  is determined by<sup>8,9</sup>

$$n(R) = \frac{1}{3\pi R_c^3 R_e} \left(\frac{R_c}{R_e}\right)^{-\frac{2}{3}} \frac{R(R_c - R^*)}{R - R^*} \frac{A_2 R + A_3}{A_2 R_c + A_3} \exp(B_1 + B_2) \quad (S4)$$

where

$$B_1 = \frac{A_2}{\tau A_1} \left[ \frac{R_c^2 - R^2}{2} + R^*(R_c - R) - R^{*2} \ln\left(\frac{R - R^*}{R_c - R^*}\right) \right] \quad (S5)$$

$$B_2 = \frac{A_3}{\tau A_1} \left[ R_c - R - R^* \ln\left(\frac{R - R^*}{R_c - R^*}\right) \right] \quad (S6)$$

$$\tau = \frac{3R_c^2 (A_2 R_c + A_3)^2}{A_1 (11A_2 R_c^2 - 14A_2 R_c R^* + 8A_3 R_c - 11A_3 R^*)} \quad (S7)$$

$$A_1 = \frac{\Delta T}{h_{fg} \rho_w (1 - \cos \theta)^2 (2 + \cos \theta)} \quad (S8)$$

$$A_2 = \frac{\theta}{4k_w \sin \theta} \quad (S9)$$

$$A_3 = \frac{1}{2h_i (1 - \cos \theta)} + \frac{1}{k_{HC} \sin^2 \theta} \left[ \frac{k_p \varphi}{\delta_{HC} k_p + h k_{HC}} + \frac{k_w (1 - \varphi)}{\delta_{HC} k_w + h k_{HC}} \right]^{-1} \quad (S10)$$

The integral in equation (S2) represents the heat flux component from droplets smaller than the coalescence length scale ( $R < R_c$ ), where direct growth by vapor accommodation at the liquid-vapor interface dominates, and neighboring droplet coalescence is absent. To account for returning jumping droplets, we modified the developed model by assuming that the droplet departure radius ( $R_c$ ) is equivalent to the coalescence length (jumping condition), however the maximum droplet size on the surface ( $R_c$ ) is larger than the departure radius due to the return of droplets *via* entrainment.

The model results were obtained using experimentally determined droplet departure radii ( $R_c = 5 \mu\text{m}$ ) and contact angles, and assuming an effective nucleation density  $N$  from previous ESEM studies of condensation on CuO surfaces.<sup>12</sup> To model the individual droplet growth more accurately for the jumping-droplet surface, the variable contact angle during the initial stages of growth was incorporated.<sup>9</sup>

## References:

1. Ma, X. H.; Zhou, X. D.; Lan, Z.; Li, Y. M.; Zhang, Y. Condensation Heat Transfer Enhancement in the Presence of Non-Condensable Gas Using the Interfacial Effect of Dropwise Condensation. *Int. J. Heat Mass Tran.* 2008, 51, 1728-1737.
2. Rose, J. W. Dropwise Condensation Theory and Experiment: A Review. *P. I. Mech. Eng. a-J. Pow.* 2002, 216, 115-128.
3. Boreyko, J. B.; Chen, C.-H. Self-Propelled Dropwise Condensate on Superhydrophobic Surfaces. *Phys. Rev. Lett.* 2009, 103, 184501.
4. Enright, R.; Miljkovic, N.; Sprittles, J.; Mitchell, R.; Nolan, K.; Thompson, C. V.; Wang, E. N. Energy Transfer During Inertial-Capillary-Driven Droplet Jumping on Superhydrophobic Surfaces. *In review* 2013.
5. Enright, R.; Miljkovic, N.; Al-Obeidi, A.; Thompson, C. V.; Wang, E. N. Superhydrophobic Condensation: The Role of Length Scale and Energy Barriers. *Langmuir* 2012, 40, 14424–14432.
6. Enright, R.; Miljkovic, N.; Dou, N.; Nam, Y.; Wang, E. N. Condensation on Superhydrophobic Copper Oxide Nanostructures. *J. Heat Transf.* 2013, 135, 091304.
7. Miljkovic, N.; Enright, R.; Nam, Y.; Lopez, K.; Dou, N.; Sack, J.; Wang, E. N. Jumping-Droplet-Enhanced Condensation on Scalable Superhydrophobic Nanostructured Surfaces. *Nano Lett.* 2013, 13, 179-187.
8. Miljkovic, N.; Enright, R.; Wang, E. N. Effect of Droplet Morphology on Growth Dynamics and Heat Transfer during Condensation on Superhydrophobic Nanostructured Surfaces. *ACS Nano* 2012, 6, 1776–1785.
9. Miljkovic, N.; Enright, R.; Wang, E. N. Modeling and Optimization of Superhydrophobic Condensation. *J. Heat Transf.* 2012, 135, 111004.
10. Kaschiev, D. *Nucleation: Basic Theory With Applications*. Butterworth Heinemann: Oxford, 2000.
11. Carey, V. P. *Liquid-Vapor Phase-Change Phenomena: An Introduction to the Thermophysics of Vaporization and Condensation Processes in Heat Transfer Equipment*. 2nd ed.; Taylor and Francis: New York, 2008; p xxii, 742 p.
12. Enright, R.; Dou, N.; Miljkovic, N.; Nam, Y.; Wang, E. N. Condensation on Superhydrophobic Copper Oxide Nanostructures. *3rd Micro/Nanoscale Heat Mass Transf. Int. Conference* 2012.